

# AVP: Physics-informed Data Generation for Small-data Learning

Jialei Chen, Yujia Xie, Kan Wang, Chuck Zhang, Mani A. Vannan, Ben Wang, and Zhen Qian

**Abstract**—Deep neural networks have achieved great success in multiple learning problems, and attracted increasing attention from the medicine community. In reality, however, the limited availability and high costs of medical data is a major challenge of applying deep neural networks to computer-aided diagnosis and treatment planning. We address this challenge with *adaptive virtual patients (AVPs)* and the associated physics-informed learning framework. Specifically, the original training dataset is fused with an additional dataset of AVPs, which are generated by a data-driven model and the associated supervision (e.g., labels) is obtained by a physics-based approach. A key novelty in the proposed framework is the bidirectional and uncoupled *generative invertible networks (GIN)*, which can extract pathophysiological features from the training medical image and generate pathophysiological meaningful virtual patients. In order to mitigate the possibly high labeling cost of physical experiments, a  $\mu$ -measure design is conducted: this allows the AVPs to not only further explore the uncertain regions, but also balance the label distribution. We then discuss the pathophysiological interpretability of GIN both theoretically and experimentally, and demonstrate the effectiveness of AVPs using a real medical image dataset, in which the proposed AVPs lower the labeling cost by 90% while achieving a 15% improvement in prediction accuracy.

**Index Terms**—Adaptive virtual patients, Computer-aided diagnosis, Data augmentation, Generative neural networks.

## 1 INTRODUCTION

THROUGH the use of deep neural networks (NN) [1], great success has been achieved in solving challenges in computer vision [2] and natural language processing [3] demonstrating superb performances that are comparable or even superior to humans. Recently, deep NNs have attracted increasing attention from the medicine community for potential applications in computer-aided diagnosis and treatment planning [4], [5]. When feeding with a *large amount* of training data, NNs have shown great success in extracting high-level features and modeling different kinds of functions *without* domain-specific knowledge. However, the key challenge to many medicine-related deep learning problems is that, while the training of deep NNs typically requires a large amount of data (at least in the thousands [6]), the available data for training in real life is often limited and expensive to collect. Furthermore, the imbalance of data

label commonly seen in medicine (e.g., rare surgical failures v.s. common surgical success) makes it more difficult to train deep NNs [7], [8]. With only small and unbalanced data available, incorporating domain-specific knowledge as a *complement* is often times imperative for multiple learning purposes.

Introducing domain-specific knowledge or physics while learning is also referred to as physics-informed learning or physics-based and data-driven modeling in literature [9], [10]. Domain-specific knowledge is usually incorporated into the optimization search and model fitting process via imposing a prior distribution for model parameters [11], [12]. Physics-based reduced-bases are also used to add the domain-specific knowledge and reduce the requirement for large amount of training data [13], [14]. However, these approaches cannot be easily adapted to deep NNs [15]. In this paper, we introduce domain-specific knowledge by an additional physics-informed virtual dataset. Specifically, the model inputs, will be generated by a standard *data-driven* model (e.g., generative models [16]), while the output labels will be obtained by a *physics-based* labeling approach. Here, it refers to in-vitro experiments [17] or computational fluid dynamics (CFD) modeling [18], by which physical principles are incorporated to enrich the dataset. The reason for generating an additional physics-informed dataset is twofold: (i) it increases the training data size to stabilize the learning process and (ii) it contains additional physical knowledge by the labeling process to improve the model performance.

However, labeling virtual data points by physics-based approaches can be quite expensive [19]. For example, it may take hours to complete one blood flow simulation case using CFD. As for in-vitro experiments, which usually require a fabrication process of the medical phantoms, it can be expensive in both time and material. Therefore, one may

- J. Chen and C. Zhang are with the H. Milton Stewart School of Industrial and Systems Engineering and the Georgia Tech Manufacturing Institute, Georgia Institute of Technology, Atlanta, GA 30332 USA  
E-mail: {jialei.chen, chuck.zhang}@gatech.edu
- K. Wang is with the Georgia Tech Manufacturing Institute, Georgia Institute of Technology, Atlanta, GA 30332 USA  
E-mail: kwang34@mail.gatech.edu
- Y. Xie is with the School of Computational Science and Engineering, Georgia Institute of Technology, Atlanta, GA 30332 USA  
E-mail: xieyujia@gatech.edu
- B. Wang is with the H. Milton Stewart School of Industrial and Systems Engineering and the School of Materials Science and Engineering, Georgia Institute of Technology and the Georgia Tech Manufacturing Institute, Atlanta, GA 30332 USA  
E-mail: ben.wang@gatech.edu
- M. A. Vannan is with the Marcus Heart Valve Center, Piedmont Heart Institute, Atlanta, GA 30309 USA  
E-mail: Mani.Vannan@piedmont.org
- Z. Qian is with the Tencent America, Medical AI Lab, Palo Alto, CA 94306 USA  
E-mail: qianzhen@tencent.com

Corresponding author: Jialei Chen and Zhen Qian.

want to conduct an *experimental design* [20], i.e., to wisely choose the virtual data points for labeling to reduce the experimental runs and, therefore, the cost. This is not an easy task, because (i) the number of virtual data points required is large (at least in the hundreds), (ii) the dimension of the data points can be high, and (iii) it is difficult to make sure the designed virtual data points make pathophysiological sense.

In order to tackle the aforementioned challenges, we propose physics-informed *adaptive virtual patients* (AVPs) to supplement the small and perhaps unbalanced dataset. Figure 1 illustrates the proposed three-step framework for AVP generation.<sup>1</sup> In the first step, a novel *generative invertible networks* (GIN) is proposed to encode the real data points to a lower dimensional feature space, in which virtual data points can be generated. This *bidirectional* mapping allows us to use the training set to shed light on the pathophysiological meaning of the feature space. In the second step, a  $\mu$ -*measure design* is proposed to smartly sample AVPs. Within the feature space, the design of AVPs is feasible and meaningful due to its more tractable dimension and pathophysiological interpretability. Furthermore, with a proper selection of the measure  $\mu$ , AVPs can be used to both explore the uncertain regions and balance the label distribution. In the third step, AVPs are generated by GIN and labeled by a physics-based approach. The physics-informed AVPs will be merged to the real training dataset to improve the learning performance. Finally, in experiments of both synthetic dataset and real medical image dataset (of aortic stenosis), We also discuss the pathophysiological meaning and invertability of the proposed GIN both theoretically and experimentally. Finally, the proposed AVPs are tested using synthetic dataset and real medical image dataset (of aortic stenosis), where a noticeably accuracy improvement of 15% ~ 20% is observed compared to the rotation data augmentation with the same training size. Perhaps more importantly, using AVPs reduces the labeling cost of almost 90%: in experiments of aortic stenosis dataset with the (training) size 126, totally 1134 AVPs are generated and labeled, which achieves similar prediction performance as a randomly generated and labeled dataset with the size 10000.

## 2 RELATED WORK

### 2.1 Data augmentation and transfer learning

For small-data learning problems with medical image inputs, *data augmentation* approaches [21] are commonly used, including image transformation and change of image tune and/or brightness. Usually, it assumes such augmentation doesn't change the label, which may not hold true in medical images [22]. Another widely used approach is *transfer learning* [23]. Adapting the models trained on nature images, researchers are able to fine-tune the pre-trained models' coefficients to address the limitation imposed by the small sample size of the medical image data. This approach explores the visual cues extracted from natural images and assumes they are also good in interpreting medical images, the rationality of which is still unclear.

1. The code is available in this repository: <https://github.gatech.edu/jchen663/HeartValveProject-GIN>.

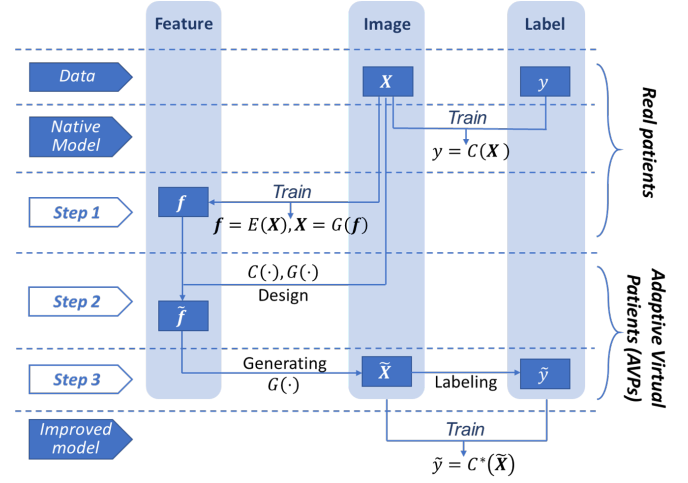


Fig. 1: The proposed three-step framework of generating, designing and labeling the adaptive virtual patients (AVP). We start with the native model  $C(\cdot)$  by the real dataset and finally, we reach to a better model  $C^*(\cdot)$  using both the real dataset and the AVPs.

### 2.2 Generative Adversarial Networks

Generative Adversarial Networks (GAN) [16] opens an era of adversarial training for multiple learning challenges, e.g., image segmentation [24] and domain adaptation [25]. It adversarially trains two NNs to obtain a one-directional generating mapping. One of its variations related to this work is conditional GAN (CGAN) [26], which generates images conditional on labels. In contrast, we will only generate the input images, while the labels will be acquired via physical experiments to accommodate the small-data situation. Another intriguing variation is adversarially learned inference (ALI) [27] or bidirectional GAN (BiGAN) [28]. They can learn both generating mapping and its inverse by a *coupled* architecture of three NNs. However, coupled training of these three NNs requires a large amount of data, which we don't have in many medicine-related problems.

### 2.3 Uniform design

For better prediction performance with limited data size, one may properly sample or *design* data points in the training set [29]. In literature, *uniform design* [30] is a model-free approach that spreads the training set uniformly in the feasible space to best survey the whole space. Specifically, the sampled points are selected such that their empirical distribution is as close as to the uniform distribution, i.e.,

$$\mathcal{D} = \underset{\mathcal{D}}{\operatorname{argmin}} \max_{z \in \mathbb{F}} \left| \sum_{i=1}^{|\mathcal{D}|} \frac{\mathcal{I}\{z_i < z\}}{|\mathcal{D}|} - F_{\mathcal{U}}(z) \right|, \quad (1)$$

where  $\mathcal{I}\{\cdot\}$  is the indicator function,  $\mathcal{D} = \{z_i\}$  is the sampled set,  $|\mathcal{D}|$  is the predefined sample size,  $F_{\mathcal{U}}(\cdot)$  is the cumulative distribution function (CDF) for uniform distribution, and maximum difference in CDF is used as the metric. Furthermore, if an initial dataset  $\mathcal{D}_1$ , i.e., real training set, is available and we want to sequentially design an

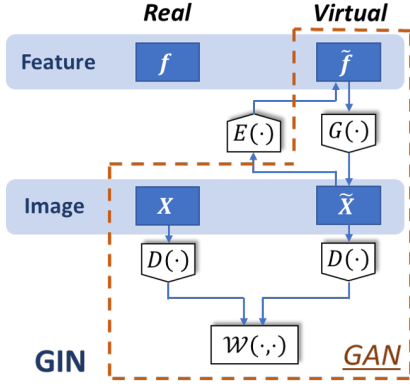


Fig. 2: The architecture of the proposed generative networks – GIN, comparing to GAN. GIN contains 3 NNs: a generator  $G(\cdot)$ , an encoder  $E(\cdot)$  and a discriminator  $D(\cdot)$ .  $G(\cdot)$  and  $D(\cdot)$  is obtained by optimizing the Wasserstein distance  $\mathcal{W}(\cdot, \cdot)$ .  $E(\cdot)$  is a sample-to-sample inverse of the  $G(\cdot)$ , explicitly trained by minimizing MSE.

additional dataset  $\mathcal{D}_2$ , i.e., virtual data points, an extension of (1) is,

$$\mathcal{D}_2 = \operatorname{argmin}_{\mathcal{D}_2} \max_{z \in \mathbb{F}} \left| \sum_{i=1}^{|\mathcal{D}_1|+|\mathcal{D}_2|} \frac{\mathcal{I}\{z_i < z\}}{|\mathcal{D}_1| + |\mathcal{D}_2|} - F_{\mathcal{U}}(z) \right|, \quad (2)$$

which makes sure the combination of both datasets  $\mathcal{D}_1 \cup \mathcal{D}_2$  is well-spread over the whole feature space and therefore, better surveying of the whole space.

### 3 GENERATIVE INVERTIBLE NETWORKS

In this section, we propose a novel generative networks – *generative invertible networks (GIN)* to generate pathophysiologically interpretable virtual data points or virtual patients. As illustrated in Figure 2, GIN embeds the images  $\mathbf{X} \in \mathbb{X}$  into a much lower-dimensional feature space  $\mathbb{F}$  by an encoding mapping  $E(\cdot) : \mathbb{X} \mapsto \mathbb{F}$ , and generates images by a generating mapping  $G(\cdot) : \mathbb{F} \mapsto \mathbb{X}$ . As for its connection to the whole proposed framework (Figure 1), GIN is learned in step 1 and is used to generate AVP in step 3.

#### 3.1 Generator

For training set images, i.e., real images, we regard them as realizations of a distribution with probability measure  $\mathcal{X} : \mathcal{B}[\mathbb{X}] \mapsto [0, 1]$  in the image space  $\{\mathbb{X}, \mathcal{B}[\mathbb{X}]\}$ , where  $\mathcal{B}[\cdot]$  is the Borel set [31]. Intuitively,  $\mathcal{X}$  is selected that for any images  $\mathbf{X}_0 \in \mathbb{X}$  of interest, its probability density function (PDF)  $f_{\mathcal{X}}(\mathbf{X}_0)$  is nonzero. The dimension of image data is usually high, i.e.,  $\dim(\mathbb{X}) = p \times q$ , but the dimension of the support, i.e.,  $\operatorname{supp}(\mathcal{X})$  should not be as high as  $\mathbb{X}$ . Usually,  $\operatorname{supp}(\mathcal{X})$  can be viewed as a much lower dimensional manifold in  $\mathbb{X}$  [1]. The objective is to mimic  $\mathcal{X}$  by a measure  $\tilde{\mathcal{X}}$  for the generated images.

Instead of learning the probability measure  $\tilde{\mathcal{X}}$  on the image space  $\{\mathbb{X}, \mathcal{B}[\mathbb{X}]\}$  from scratch, we learn a generating mapping  $G(\cdot) : \mathbb{F} \mapsto \mathbb{X}$ . Therefore, one may regard  $\tilde{\mathcal{X}}$  as a pushforward of a much simpler measure  $\mathcal{U}$  on measurable space  $\{\mathbb{F}, \mathcal{B}[\mathbb{F}]\}$ , i.e.,  $\tilde{\mathcal{X}} = G_{\#}(\mathcal{U})$ . Here, we choose  $\mathcal{U}$  to be

the uniform distribution on a simple rectangular support  $\operatorname{supp}(\mathcal{U}) = \mathbb{F} = [-1, 1]^r$ , where  $r$  is a hyperparameter as a conjecture for the dimension of  $\operatorname{supp}(\mathcal{X})$ . We regard the low-dimensional space  $\mathbb{F}$  as the *feature space*, whose pathophysiological meaning will be endowed later in Section 3.2. Therefore, one can generate pathophysiologically meaningful virtual patients from  $\mathbb{F}$ , rather than some images that look like patients with unknown pathophysiological interpretation. Furthermore,  $\mathbb{F}$  has much lower dimension than  $\mathbb{X}$ , which offers the possibility of the downstream applications, e.g., designing AVPs (see Section 4.1).

We find  $\tilde{\mathcal{X}} = G_{\#}(\mathcal{U})$  by minimizing its distance to the ground truth  $\mathcal{X}$ . Wasserstein-1 distance [32] is introduced as the metric:

$$\mathcal{W}(\mathcal{X}, \tilde{\mathcal{X}}) = \inf_{\gamma} \int_{\mathbb{X} \times \mathbb{X}} \|\mathbf{X} - \tilde{\mathbf{X}}\|_2 d\gamma(\mathbf{X}, \tilde{\mathbf{X}}), \quad (3)$$

where  $\|\cdot\|_2$  is the  $l_2$  norm, and the infimum is obtained with respect to all the possible joint distribution  $\gamma : \mathcal{B}[\mathbb{X}] \times \mathcal{B}[\mathbb{X}] \mapsto [0, 1]$  whose marginals are  $\mathcal{X}$  and  $\tilde{\mathcal{X}}$ , respectively. Wasserstein distance is widely used to measure the distance between distributions, because it properly takes into account of the different supports without diverging to infinity as, for example, the K-L divergence [33]. There are lots of fast computing algorithms developed for Wasserstein distance [34], [35] in literature. Here, we adopt the Kantorovich-Rubinstein dual form [32] of Wasserstein distance,

$$\mathcal{W}(\mathcal{X}, \tilde{\mathcal{X}}) = \sup_{\|D(\cdot)\|_L \leq 1} \mathbb{E}_{x \sim \mathcal{X}}[D(x)] - \mathbb{E}_{\tilde{x} \sim \tilde{\mathcal{X}}}[D(\tilde{x})], \quad (4)$$

where  $D(\cdot) : \mathbb{X} \mapsto \mathbb{R}$  is an evaluating function and  $\|D(\cdot)\|_L \leq 1$  represents that function  $D(\cdot)$  is Lipschitz-1 continuous [36].

We use a NN to approximate the generating mapping  $G(\cdot)$ , named the *generator*, and another NN for the evaluating function  $D(\cdot)$ , named the *discriminator*. The aim is to find the optima of the following minimax function,

$$\min_{G(\cdot)} \max_{D(\cdot)} \mathbb{E}_{x \sim \mathcal{X}_n}[D(x)] - \mathbb{E}_{u \sim \mathcal{U}}[D(G(u))], \quad (5)$$

where  $\mathcal{X}_n$  is the target empirical measure for the training images of size  $n$ , and  $\mathcal{U}$  is the uniform measure to be pushforwarded. Iterative training strategy can be adapted. Further discussion on the numerical implementation and the convergence analysis can be found in Section 3.3.

#### 3.2 Encoder

We defined the feature space  $\mathbb{F} = [-1, 1]^r$  in Section 3.1 and assume for now the generating mapping  $G(\cdot)$  is known. We are interested in finding an encoding mapping  $E(\cdot) : \mathbb{X} \mapsto \mathbb{F}$  to embed the images back to the feature space, which, as we will show later in Theorem 1, is an inverse of  $G(\cdot)$ . Similar to the generating mapping, we use a NN to parametrize  $E(\cdot)$ , named the *encoder*. Since the task here is to extract the feature vectors from images, a convolutional neural network (CNN) is used with mean square error (MSE) loss:

$$E(\cdot) = \operatorname{argmin}_{E(\cdot)} \mathbb{E}_{\mathbf{X} \sim \mathcal{X}} [\|\mathbf{E}(\mathbf{X}) - \mathbf{f}\|^2], \quad (6)$$

where  $\mathbf{f} \in \mathbb{F}$  is the corresponding feature vector associated with the image  $\mathbf{X}$ . Here, the difficulty is that the feature  $\mathbf{f}$

for real patients  $\mathbf{X}$  is unknown. In other words,  $E(\cdot)$  cannot be learned from the dataset of real patients at hand.

However, as for virtual patients, we know their features since they are generated as follows: we first choose the feature  $\mathbf{f}$  and then feed them into the generator and get the virtual images  $\tilde{\mathbf{X}} = G(\mathbf{f})$ . Furthermore, as we will show later in Theorem 2, the virtual images are of the same distribution as, i.e., statistically indistinguishable from, the real ones. Thus,  $E(\cdot)$  can be learned from virtual images:

$$E(\cdot) = \underset{E(\cdot)}{\operatorname{argmin}} \mathbb{E}_{u \sim \mathcal{U}} [E(G(u)) - u]^2, \quad (7)$$

where  $\tilde{\mathbf{X}} = G(u)$  is the generated virtual patients. Another advantage of using the virtual data points is that the amount of the virtual patients can be large, since one may generate as many virtual patients  $\tilde{\mathbf{X}}$  as needed. We expect the encoder  $E(\cdot)$  learned by (7) using *virtual* data points (instead of the *real* patients) is still the inverse of the generator  $G(\cdot)$ . Formally, we have the following Theorem:

**Theorem 1.** Denote the target distribution measuring as  $\mathcal{X}$  on image space  $\{\mathbb{X}, \mathcal{B}[\mathbb{X}]\}$ . Assume the generator  $G(\cdot)$  is obtained by (5) with the training error  $< \epsilon$  and encoder  $E(\cdot)$  is obtained by (7) with the training error  $< \delta$ . If both  $G(\cdot)$  and  $E(\cdot)$  is Lipschitz- $L$  continues, then the reconstruction error  $\mathbb{E}_{x \sim \mathcal{X}} [G(E(x)) - x]^2$  can be bounded by  $(L^2 + L + 1)\epsilon + L\delta$ .

A proof can be found in Appendix A. This means  $G(\cdot)$  and  $E(\cdot)$  learned using the proposed approaches are inverses of each other in the sense of minimizing the reconstruction error.

The reason for introducing the encoding mapping  $E(\cdot)$ , or the inverse of generating mapping is twofold. First, we can encode the real images as vectors in feature space  $\mathbb{F}$ . They can then be used as the lighthouse in  $\mathbb{F}$ , and endow the space with pathophysiological meaning. Therefore, when generating virtual patients for a specific clinical purpose is required, we can pick the ones with the features in specific regions in  $\mathbb{F}$ . For example, physicians may be interested in studying the medical images that have a high probability of resulting in severe post-surgical complications, for the purpose of improving surgical success rates. Then, the regions (in  $\mathbb{F}$ ) near the real patients with severe post-surgical complications maybe the right location to explore. Second, in the later design step, we sample the AVPs for better modeling performance with limited labeling budget (see Section 4.1). It is important to note that this can only be done in  $\mathbb{F}$  rather than the image space  $\mathbb{X}$ , for its lower dimension (see Section 1). Moreover, while designing AVPs, we need the features of the real image to guide the design of AVPs. For example, one may want the features of AVPs away from the features of real patients to better explore the whole  $\mathbb{F}$ .

### 3.3 Summary and algorithm for GIN

Putting everything together, the proposed GIN consists of three NNs: a generator  $G(\cdot)$  for generating virtual patients, an encoder  $E(\cdot)$  for feature embedding, and a discriminator  $D(\cdot)$  for computing the Wasserstein distance. Figure 2 illustrates the architecture of GIN. Note that in GIN,  $G(\cdot)$  and  $E(\cdot)$  is decoupled due to the limited data available.

#### Algorithm 1 Generative invertible networks

---

```

1: procedure GIN( $\{\mathbf{X}_i\}_{i=1}^n$ )
2:   Initialize  $G_\theta(\cdot)$ ,  $D_w(\cdot)$ , and  $E_\gamma(\cdot)$ 
3:   while  $\theta$  has not converged do
4:     for  $t = 0, \dots, n_d$  do
5:       Sample  $\{\mathbf{X}_i\}_{i=1}^m$  a batch from the real data.
6:       Sample  $\{\mathbf{f}_i\}_{i=1}^m \sim \mathcal{U}$ 
7:        $L_D = \sum_{i=1}^m D_w(\mathbf{X}_i) - \sum_{i=1}^m D_w(G_\theta(\mathbf{f}_i))$ 
8:        $w = w + \alpha \nabla L_D$ 
9:        $w = \text{clip}(w, -\beta, \beta)$ 
10:      Sample  $\{\mathbf{f}_i\}_{i=1}^m \sim \mathcal{U}$ 
11:       $L_G = -\sum_{i=1}^m D_w(G_\theta(\mathbf{f}_i))$ 
12:       $\theta = \theta - \alpha \nabla L_G$ 
13:     $G(\cdot) = G_\theta(\cdot)$ 
14:    while  $\gamma$  has not converged do
15:      Sample  $\{\mathbf{f}_i\}_{i=1}^m \sim \mathcal{U}$ 
16:      Generate  $\{\mathbf{X}_i = G_\theta(\mathbf{f}_i)\}_{i=1}^m \sim \tilde{\mathcal{X}}$ 
17:       $L_E = \sum_{i=1}^m (E_\gamma(\mathbf{X}_i) - \mathbf{f}_i)^2$ 
18:       $\gamma = \gamma - \alpha \nabla L_E$ 
19:     $E(\cdot) = E_\gamma(\cdot)$ 
20:  return  $G(\cdot)$ ,  $E(\cdot)$ 

```

---

We propose Algorithm 1 to train the GIN. The first part of the algorithm aims to train a generator  $G(\cdot)$  parameterized by  $\theta$ . In each iteration, we first conduct a stochastic gradient descent (SGD) on  $D(\cdot)$  parameterized by  $w$ , to find the optimal  $D(\cdot)$  under current  $G_\theta(\cdot)$ . Note for each update, we clip  $w$  into  $[-\beta, \beta]$ , so the Lipschitz constraint is satisfied [36]. Then we sample a batch of features to conduct SGD on  $G(\cdot)$ . The second part of the algorithm aims to find an encoder  $E(\cdot)$  parameterized by  $\gamma$ . In each SGD iteration, we generate a batch of images  $\{\tilde{\mathbf{X}}_i = G(\mathbf{f}_i)\}_{i=1}^m$  using sampled features  $\{\mathbf{f}_i\}_{i=1}^m$ . Then we encode the generated images back to the feature space  $\mathbb{F}$  using  $E(\cdot)$ , and compare the encoded  $\{E(\tilde{\mathbf{X}}_i)\}_{i=1}^m$  to  $\{\mathbf{f}_i\}_{i=1}^m$  using MSE loss.

One may be interested in finding out how real virtual patients can be generated using the proposed Algorithm 1, since multiple heuristic strategies are involved (e.g., iterative training of  $D(\cdot)$  and  $G(\cdot)$ , and clip). Furthermore, note that the above computation is done with samples of real images, i.e., the *empirical* probability measure, instead of the original probability measure. Nevertheless, we have the following theorem to guarantee the asymptotic convergence.

**Theorem 2.** Denote the target measure as  $\mathcal{X}$  and its empirical measure represented by the training set data as  $\mathcal{X}_n$ . Assuming both neural networks  $G(\cdot)$  and  $D(\cdot)$  are obtained as the optima of target function (5). Denoting  $\tilde{\mathcal{X}}$  as the measure obtained by the proposed Algorithm 1. It is a pushforwarded measure of  $\mathcal{U}$  by  $G(\cdot)$ , i.e.,  $\tilde{\mathcal{X}}[S] = (G_\#(\mathcal{U}))[S] = \mathcal{U}[G^{-1}(S)]$  for any  $S \in \mathcal{B}[\mathbb{X}]$ . As the training data size approaches infinity, we have  $\tilde{\mathcal{X}} \rightarrow \mathcal{X}$  in distribution.

A proof can be found in Appendix B. This suggests that, if we have enough training data, the generated images are *real* enough compared to the real images. Specifically, it means generated images and their measure have the following two properties. First and most importantly, the support of the two measures are the same, i.e.,  $\text{supp}(\tilde{\mathcal{X}}) = \text{supp}(\mathcal{X})$ ,

with probability one. This is a natural corollary of Theorem 2, which means any generated virtual image  $\tilde{\mathbf{X}}$  can be regarded as a draw from the measure of real patients  $\mathcal{X}$ , i.e.,  $f_{\mathcal{X}}(\tilde{\mathbf{X}}) > 0$ , where  $f_{\mathcal{X}}(\cdot)$  denotes the PDF of  $\mathcal{X}$ . In other words, the generated images are always pathophysiological meaningful. Moreover, besides their support, the two probability measures themselves are the same asymptotically. This means the probability of generating the same group of images (e.g., images of male patients, or images of patients with no complications) is the same, which is an implicit requirement when endowing the feature space with pathophysiological meaning and for later designing AVPs.

#### 4 ADAPTIVE VIRTUAL PATIENTS

We propose the adaptive virtual patients (AVPs) and the associated learning framework (see Figure 1) to address the small data problem. Here, we assume the learning task to be a *classification* problem with inputs of medical images  $\mathbf{X}_i \in \mathbb{X}$ . It is important to note the proposed framework can be easily extended to regression tasks, which will not be elaborated on in this paper. Denote the label, i.e., the classification output as  $y_i \in \{0, 1\}$ . We are interested in finding a classifier, approximated by a NN, to model the probability of class  $y = 1|\mathbf{X}$ . As illustrated in Figure 1,  $C(\cdot) : \mathbb{X} \mapsto [0, 1]$  is referred to as a native model learned from the real dataset. The proposed framework contains three steps: (i) GIN is trained with the encoding mapping  $E(\cdot)$  and the generating mapping  $G(\cdot)$ ; (ii) the features of real patients are acquired by  $E(\cdot)$  and AVPs are designed focusing on the uncertainty regions of  $C(\cdot)$  and (iii) AVPs are generated by  $G(\cdot)$  and labeled using a physics-based approach. By merging the real dataset  $\mathbf{X}_i$  and physics-informed AVPs  $\tilde{\mathbf{X}}_j$ , a better classifier  $C^*(\cdot)$  can be learned.

Since GIN and the associated Algorithm 1 were proposed in Section 3, we will focus on the remaining two steps, i.e., designing and labeling in this section. Finally, Algorithm 2 will be proposed for the whole learning framework.

##### 4.1 $\mu$ -measured Design

We first proposed a novel design approach by incorporating prior knowledge, i.e., the classification uncertainty of the native model  $C(\cdot)$ . As shown in Section 2.3, uniform design can be formulated in an optimization (2). Here, we want to replace the uniform measure  $\mathcal{U}$  with a new measure  $\mu$  representing the uncertainty of  $C(\cdot)$ . To this end, apart from the space-filling property, we also expect the designed AVPs to focus on the uncertain regions of  $C(\cdot)$ .

We define the uncertainty measure  $\mu : \mathcal{B}(\mathbb{F}) \mapsto [0, 1]$  by its PDF:

$$f_{\mu}(z) = b \exp(-\theta[C(G(z)) - TH]^2) \quad \text{for } \forall z \in \mathbb{F}, \quad (8)$$

where  $\theta$  is the hyperparameter,  $b$  is the integral constant and  $TH \in [0, 1]$  is a pre-defined threshold for  $C(\cdot)$ . Intuitively, when the prediction result  $C(G(z))$  approaches  $TH$ , i.e., the decision boundary, the uncertainty density  $f_{\mu}(z)$  increases. While the prediction is away from the  $TH$ , the density decreases exponentially with a tuning rate of  $\theta$ . Note that the definition of the uncertainty measure shown in (8) is used specifically for a classification problem. Again, the

proposed approach is also suitable for regression problems via a different formula for the uncertainty measure. For example, one may learn the measure from the training error using kernel regression [37] or kriging [38] methods.

Now we replace the uniform measure in Equation (2) to the newly defined uncertainty measure  $\mu$ , and formulate the following  $\mu$ -measure sequential design problem:

$$\tilde{\mathcal{D}} = \arg \min_{\tilde{\mathcal{D}}} \max_{\mathbf{f} \in \mathbb{F}} \left| \sum_{i=1}^{|\mathcal{D}|+|\tilde{\mathcal{D}}|} \frac{\mathcal{I}\{\tilde{\mathbf{f}}_i < \mathbf{f}\}}{|\mathcal{D}|+|\tilde{\mathcal{D}}|} - F_{\mu}(\mathbf{f}) \right|, \quad (9)$$

where  $F_{\mu}(\cdot)$  is the CDF associated with the measure  $\mu$ ,  $\mathcal{D}$  is the set of features of real patients, i.e.,  $\mathcal{D} = \{E(\mathbf{X}_i)\}_{i=1}^n$ , and  $\tilde{\mathcal{D}} = \{\tilde{\mathbf{f}}_i\}$  is the set of features of AVPs to be optimized. The AVPs  $\tilde{\mathbf{X}}$  can then be easily acquired by the generating mapping  $G(\cdot)$ , i.e., for  $\forall \tilde{\mathbf{f}} \in \tilde{\mathcal{D}}$ ,  $\tilde{\mathbf{X}} = G(\tilde{\mathbf{f}})$ . It is important to note that the optimization (9) is conducted in the feature space  $\mathbb{F}$  rather than the image space  $\mathbb{X}$ , because (i) it has a much lower dimension, and (ii) designing in  $\mathbb{F}$  and then using  $G(\cdot)$  to generate images can ensure that the designed AVPs are pathophysiological meaningful. Meanwhile, the design is possible only when the both the generating mapping  $G(\cdot)$  and the encoding mapping  $E(\cdot)$  are acquired by GIN (see Section 3). Similar ideas in the statistics community are referred to as the adaptive sampling [39] or adaptive experimental design [40].

##### 4.1.1 Sampling AVPs

One problem is that the objective function (9) is non-continuous due to the empirical CDF represented by the design points. This is difficult to solve with simple approaches, e.g., gradient descent and quasi-Newton methods. Alternatively, we utilize support points (SP) [41], i.e., instead of optimizing the points so that their empirical distribution is close enough to target one, we directly sample the representation points from the target measure  $\mu$ . One appealing fact of SPs, different from the other sampling method, like the Markov chain Monte Carlo (MCMC [42]), is that it introduces a negative correlation to the selected points so that they are separated apart from one another. This aligns with the space-filling property of the  $\mu$ -measure design. The rationality for using SPs is that the sampled points follow the target measure  $\mu$ . This can be stated in the following theorem.

**Proposition 1.** *Let target distribution be  $\mu$  and the empirical distribution of  $\mathcal{D}_n$  with  $n$  design points or support points is  $\hat{\mu}_n$ , then  $\hat{\mu}_n \rightarrow \mu(\cdot)$  in distribution*

The proof can be found in [41], and further discussion can be found in [43]. Note that again, the SP sampling is conducted in the feature space  $\mathbb{F}$ .

The key motivation of the  $\mu$ -measure design proposed in (9) and implemented by SPs is to reduce the physical labeling (e.g., in-vitro experiments) runs and cost. Specifically, the sampled AVPs enjoy the following advantages: (i) they are away from each other to reduce repetition or redundancy, (ii) they are separated from real patients to avoid wasting any experimental run, and (iii) they are designed to focus on the decision boundary (where the uncertainty of the native model is high) for better surveying of the uncertain regions. The advantages above will help on

improving the classification performance even with a small amount of AVPs.

#### 4.1.2 Balancing the label distribution

Besides the advantages of reducing cost for later experiments, the proposed  $\mu$ -measure design (implemented by SPs) can also be used to balance the label distribution. To this end, in a binary classification scenario, a proper modification of the measure  $\mu$  is needed:

$$f_\mu(z) = \begin{cases} b_1 \exp(-\theta_1(c(z) - TH)) & \text{if } c(z) \geq TH; \\ b_0 \exp(-\theta_0(c(z) - TH)) & \text{if } c(z) < TH, \end{cases} \quad (10)$$

where the notation  $c(z) = C(G(z))$  is only for simplification,  $\theta_1$  and  $\theta_0$  are the hyperparameters controlling the decaying speed within two classes, and  $b_1$  and  $b_0$  are the integral constants.

If we choose the hyperparameters  $\theta_1, \theta_2$  and the associated integral constants  $b_1, b_2$  such that,

$$\int_{\mathbb{F}_0} f_\mu(z) dz = \int_{\mathbb{F}_1} f_\mu(z) dz = \frac{1}{2}, \quad (11)$$

where, subset  $\mathbb{F}_0 = \{z \in \mathbb{F} : C(G(z)) < TH\}$  and subset  $\mathbb{F}_1 = \{z \in \mathbb{F} : C(G(z)) \geq TH\}$ . The new  $\mu$ -measure design can balance the label distribution. Specifically, we have the following Theorem.

**Theorem 3.** Assume we set the hyperparameters  $\theta_1, \theta_2$  and select  $b_1, b_2$  in  $\mu$  such that Equation (11) holds. Denote the original real dataset as  $\mathcal{D} = \{E(\mathbf{X}_i)\}_{i=1}^n$ , and the AVPs generated by sequential SPs following  $\mu$  as  $\tilde{\mathcal{D}} = \{\tilde{\mathbf{f}}_i\}$ , then

$$\lim_{m \rightarrow \infty} \frac{\sum_{i \in \mathcal{D} + \tilde{\mathcal{D}}} \mathcal{I}(C(\mathbf{X}_i) > TH)}{\sum_{i \in \mathcal{D} + \tilde{\mathcal{D}}} \mathcal{I}(C(\mathbf{X}_i) < TH)} = 1, \quad (12)$$

where,  $m = |\tilde{\mathcal{D}}|$  is the number of the AVPs,  $C(\cdot)$  is the native classifier with classification threshold  $TH$ .

A proof using Proposition 1 and Equation (11) can be found in Appendix C.

To summarize the  $\mu$ -measure design process, the first step is to model the native classifier  $C(\cdot)$  by a CNN. Then, it can be transformed to the density of measure  $\mu$  by (8) if there is no severe unbalance or by (10) if there is. Finally, AVPs can be sampled using SPs from  $\mu$ . With the proposed strategies, the designed AVPs not only focus more on the uncertainty region but also balance the label distribution if needed.

## 4.2 Labeling by physical principle

As discussed in Section 1, a key novelty of this paper, compared to data augmentation or other generative model work, is that we try to incorporate the physical knowledge into the labels of AVPs for medicine-related learning problems with a small data size.

In this work, we separate the input medical image and the output label. We use a data-driven approach, i.e., the proposed GIN (see Section 3) with a  $\mu$ -measure design (see Section 4.1) to generate AVPs, while using a physics-based approach, e.g., in-vitro experiments [44] to obtain the label. Other physics-based approaches can also be used. For example, one may adapt empirical models (e.g., labeling

## Algorithm 2 Improving prediction by AVPs

- 1: **Native model**
- 2: Train CNN,  $C(\cdot) = \text{CNN}(\{\mathbf{X}_i\}_{i=1}^n, \{y_i\}_{i=1}^n)$
- 3: **Step 1: Generating**
- 4: Set the feature space  $\mathbb{F} = [-1, 1]^r$
- 5: Train GIN,  $G(\cdot), E(\cdot) = \text{GIN}(\{\mathbf{X}_i\})$
- 6: **Step 2: Designing**
- 7: Features of the real patients,  $\mathbf{f}_i = E(\mathbf{X}_i)$
- 8: **for**  $i=1, \dots, n$  **do**
- 9:   Obtain the prediction on real patients,  $\hat{y}_i = C(\mathbf{X}_i)$
- 10:   Obtain measure density on feature of real patients,  $f_\mu(\mathbf{f}_i) = b \exp[-\theta(\hat{y}_i - TH)^2]$ ,
- 11: Interpolating, normalizing and balancing the measure  $\mu$
- 12: Markov Chain Monte Carlo,  $\{s_k\} = \text{MCMC}(\mu)$
- 13: Sequential support points sampling,  $\tilde{\mathbf{f}}_j = \text{SP}(\{s_k\} | \mathbf{f}_i)$
- 14: **Step 3: Labeling**
- 15: Obtain AVP,  $\tilde{\mathbf{X}}_j = G(\tilde{\mathbf{f}}_j)$ ,  $j = 1, 2, \dots, m$
- 16: Obtain labels,  $\tilde{y}_j$  of  $\tilde{\mathbf{X}}_j$  by physical approaches
- 17: **Improved model**
- 18: Train CNN,  $C^*(\cdot) = \text{CNN}([\{\mathbf{X}_i\}, \{\tilde{\mathbf{X}}_j\}], [\{y_i\}, \{\tilde{y}_j\}])$
- 19: Comparing the performance of  $C(\cdot)$  and  $C^*(\cdot)$

by doctor's experience or simple pathophysiological relationship) or simulation models (e.g., finite element [45] and computational fluid dynamics [18]). The specific approach should be made on a case-by-case basis, with the available resources at hand. Meanwhile, it is important to note that these labeling approaches are usually expensive. For example, it may take several hours of computation for a CFD model with complex geometry [18] and it would be even longer if considering the interaction of blood flow and soft biological tissue [46]. This is one of the reasons for introducing the  $\mu$ -measure design for AVPs.

## 4.3 Method summary and Algorithm 2

In summary, we propose a physics-based and data-driven framework to generate AVPs and improve the classification accuracy with only limited data available. As illustrated in Figure 1, the proposed framework contains three steps, assuming the native model  $C(\cdot)$  has already been obtained. First, the proposed GIN, i.e., a generating mapping  $G(\cdot)$  and an encoding mapping  $E(\cdot)$  (one is the inverse of the other, see Theorem 1) are obtained to generate pathophysiologically meaningful (see Theorem 2) virtual patients. Second, a  $\mu$ -measure design is conducted based on the uncertainty of  $C(\cdot)$  in the feature space  $\mathbb{F}$ . It is implemented by SPs (see Proposition 1) and can also be used to balance the label distribution (see Theorem 3). Third, pathophysiological interpretable AVPs are generated and labeled by a physics-based approach (e.g., in-vitro experiments). Finally, the generated AVPs (both medical images and the associated labels) are merged with the training set of the real patients, and an improved classifier  $C^*(\cdot)$  can be trained with better classification accuracy.

In order to put the above framework in practice, we propose Algorithm 2. Note if the data set at hand is too small or unbalanced, the native model and the GIN using only the real dataset may be unstable. Several iterations of Algorithm 2 are recommended for better performance.



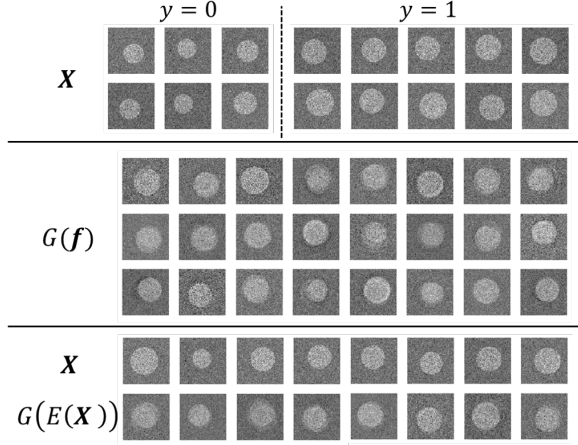


Fig. 3: Qualitative results for GIN training using synthetic data, including the training set data  $X$  with different label, generated samples  $G(f)$ , real data  $X$  and the corresponding reconstructions  $G(E(X))$ .

## 5 EXPERIMENTS

### 5.1 Experiments on synthetic medical data

We first conduct experiments on synthetic data. The synthetic dataset is generated to approximate the CT images with a circular object – such as a tumor – inside the images (see Figure 3). Here, we want to classify whether the radius of the object is greater than the threshold. Related to the real-world applications, this task can be interpreted as classifying the size of a tumor [47] or identifying the head size of a fetus [48]. The training dataset is designed to be both small ( $n = 600$ ) and unbalanced (size of classes, 11 : 1).

#### 5.1.1 Synthetic dataset

The dataset was generated as follows. Within the randomly selected circular region, the pixel intensity was increased by a uniform random variable ( $\sim \mathcal{U}[0, 0.5]$ ). Then, Gaussian background noise was added with a randomly generated mean ( $\sim \mathcal{U}[0, 1/6]$ ) and variance  $\sigma^2 = 1/4$ . The visual result is a brighter circle presented on a darker background at a variant location and with a variant noise level. The radius of the circle is dichotomized into two classes: one is greater than 20 pixels and the other is less than 20 pixels. Figure 3 shows some representative synthetic images of the two classes.

This classification task is not as easy as one may expect. If we have enough data, as assumed by most of the literature, a relatively *complex* and deep NN can be learned with good prediction performance reported [2], [15]. However, with limited data available, a NN with only *low* complexity should be used. Factoring the difficulties induced by the Gaussian background noise with *random* mean, the classification accuracy using NN can be low (see Section 5.1.3).

#### 5.1.2 Interpretability of GIN

We test the proposed generative network – GIN. The dimension of the feature space is set to be  $r = 2$ , i.e.,  $\mathbb{F} = [-1, 1]^2$ , for better visualization purpose. Detailed architecture of the three NNs can be found in Appendix D. Note that the complexity of  $E(\cdot)$  is much higher than the  $G(\cdot)$  and  $D(\cdot)$ . It

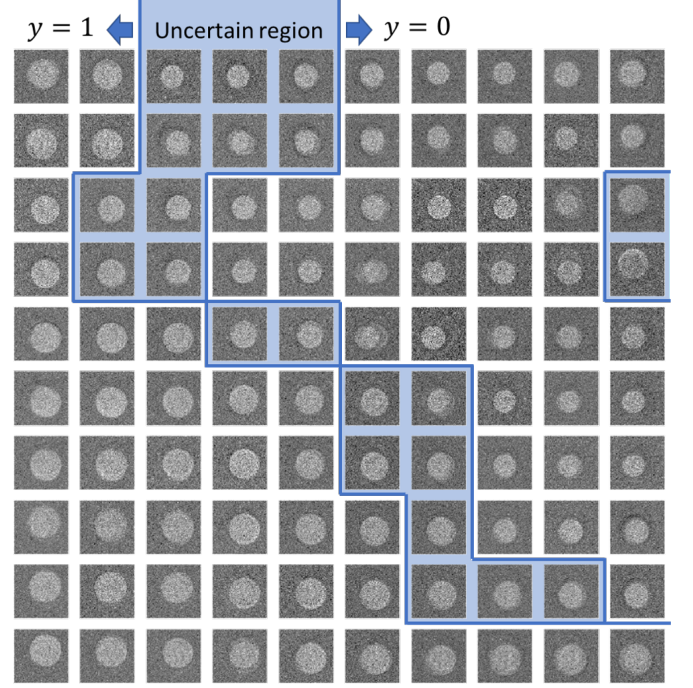


Fig. 4: Qualitative visualization of 2D sub-feature space with the generated virtual images on the grid of feature space. The bottom left region contains a big circle (i.e., class  $y = 1$ ), while the top right region contains a small circle (i.e., class  $y = 0$ ).

is to make sure  $E(\cdot)$  can reverse  $G(\cdot)$  in practice. Meanwhile, as far as we have observed, there is no obvious overfitting. This is because that the dataset of generated virtual patients is used to train  $E(\cdot)$ , and its size is large (see Section 3.2).

**Interpreting feature space.** The low-dimensional feature space  $\mathbb{F} = [-1, 1]^2$  can be visualized as follows: a uniform grid in  $\mathbb{F}$  is used and the generated virtual images at different grids are listed at their feature location. Figure 4 visualizes the sub-feature space (i.e.,  $(-0.5, 0.5]^2 \subset \mathbb{F}$ ). The total 100 generated virtual images show the continuity of  $\mathbb{F}$ , i.e., for any vertical or horizontal group of 10 images, both the location and the size of the circle are gradually changed. However, this change is not monotone. For example, in the left vertical group of images, the circle size changes from big to relatively small and back to big again. This is mainly because the dimension  $r = \dim(\mathbb{F}) = 2$  is not big enough to represent only one feature in each dimension. Furthermore, even with this small  $r$ ,  $\mathbb{F}$  seems to capture the most important feature of interest – the size of the circle. As shown in Figure 4, the bottom left region seems to only contain a big circle (i.e., the class  $y = 1$ ), while the top right region only contains a small circle (i.e., the class  $y = 0$ ). The uncertain region, however, mostly lays in between. Note that the above separation of the two classes is a heuristic way to show the physical meaning of  $\mathbb{F}$  and cannot be used for later classification.

**Reconstruction test.** Figure 5 illustrates the following reconstruction test: given any real image  $X_i$ , its feature is extracted  $f_i = E(X_i)$ , and then a reconstructed image can be generated based on that feature  $G(f_i) = G(E(X_i))$ . Note that we have already proven that the two mapping

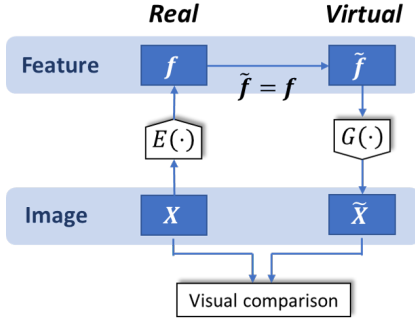


Fig. 5: Illustration of reconstruction test.

$G(\cdot)$  and  $E(\cdot)$  are inverses of each other in an ideal situation (see Theorem 1), and that this test is a comparison to find practical similarities. The last row of Figure 3 compares the real image  $X_i$  and the reconstructed ones  $G(E(X_i))$  visually. The similarity between  $X$  and  $G(E(X))$  is noticeable, especially when we focus on the location and the size of the circle. However, the reconstructed images and the original ones are not identical and the generated images are not as sharp as the real images. This is attributable to the fact that the training set only contains a very small amount of data points and only the local optimum can be reached in practice.

### 5.1.3 Improving accuracy by AVPs

Now we test the proposed AVPs in improving the classification accuracy with this small and unbalanced dataset. The testing set contains 100 data points with 50 data points of either classe. A CNN  $C(\cdot)$  is used as the vanilla native model with a detailed architecture specified in Appendix D. Table 1 reports its accuracy together with the sensitivity (true positive rate, i.e., accuracy when the ground truth is 1) and the specificity (true negative rate, i.e., accuracy when the ground truth is 0) on the testing set. The classification accuracy of the vanilla native model is only  $\sim 60\%$ . This is not surprising, since the CNN is not complex enough due to the limited training dataset as discussed in Section 5.1.1.

Two standard methods for modeling unbalanced data are used including an *under-sampling* strategy, i.e., removing the data points in the larger class, and an *over-sampling* strategy, i.e., augmenting the data points in the smaller class by adding constants to every pixel. The testing accuracy, sensitivity and specificity are also reported in Table 1. Compared with the vanilla native model, these two sampling strategies improve the accuracy marginally. Using the under-sampling strategy, since we are removing data points from the already limited training set, the balance between the sensitivity and the specificity are slightly improved but the absolute values are still low. For the over-sampling method, the sensitivity and specificity are still unbalanced, because simple data augmentation is not an ideal way to balance the label distribution.

**Sampling AVPs.** In this test, the objective for the proposed  $\mu$ -measure design is to both explore the uncertainty regions and balance the label distribution. Thus, Equation (10) is used to formulate the density  $f_\mu(\cdot)$ . The selection of hyperparameters in (10) is discussed in Appendix D. Two

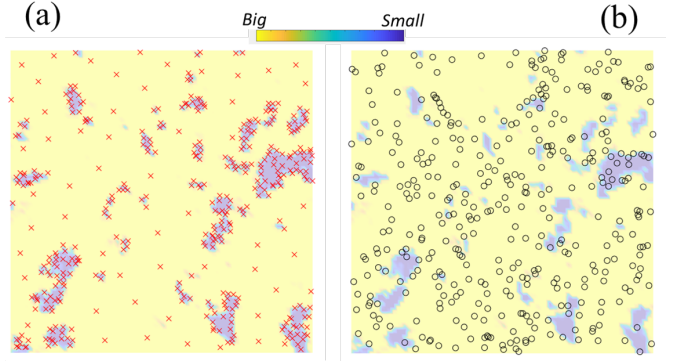


Fig. 6: A comparison of well-designed AVP (total 600) and the random sampling (first 600 out of 1800) in the feature space  $\mathbb{F}$ . The background is the prediction contour of the native model  $C(G(\cdot))$ .

datasets of AVPs with the size 600 and 1800 are generated. In addition, a random sampling over the feature space of 1800 virtual patients is also generated as a baseline test.

Figure 6 (a) visualizes the designed AVPs (a total of 600) in the 2D feature space  $\mathbb{F}$ . As a comparison, Figure 6 (b) visualizes the random sampled virtual patients (first 600 out of 1800). The background of Figure 6 is the prediction contour of the vanilla native model  $C(\cdot)$  in  $\mathbb{F}$ , i.e.,  $C(G(\cdot)) : \mathbb{F} \mapsto [0, 1]$ . We can see that the contour of the prediction  $C(G(\cdot))$  indicates a clear unbalance, i.e., the blue regions of class  $y = 1$  is much smaller in area than the yellow regions of class  $y = 0$ . AVPs (red crosses in Figure 6) enjoy the following properties: (i) AVPs help balance the dataset by sampling more data points at the blue regions than the yellow regions; (ii) a portion of AVPs lay on the decision boundary, where the uncertainty of the native model is high; (iii) the AVPs are well-spread out to better survey the whole  $\mathbb{F}$ , which is especially clear in the yellow regions. On the contrary, almost all of the random sampled virtual patients (black circles in Figure 6) located in the yellow regions and very few in the blue regions, which indicates little improvement in balancing the label distribution. Also, clear voids in some regions of  $\mathbb{F}$  and overlapping in other regions are observed, which means that the first 600 random sampling data points are neither exploring the whole  $\mathbb{F}$  nor efficient without waste. When the number of the random virtual patients increase to 1800 the voids will be less but will still exist, but more importantly, it is more expensive for the later labeling process.

**Labeling AVPs.** The three virtual datasets (600 AVPs, 1800 AVPs and random sampled with size 1800) are generated by generating mapping  $G(\cdot)$  from the acquired features. Then they are labeled by a thresholding method reported in [49], i.e., an optimal threshold is obtained for each virtual data point by maximizing the excess entropy. Finally, the labeling results are manually checked and corrected if needed.

**Classification accuracy.** The three datasets generated are fused with a real dataset for training three different classifiers, respectively. The architecture of the improved classifiers are set to be the same as the native model (see Appendix D). Table 1 summarizes the classification accuracy



TABLE 1: A comparison of classification sensitivity, specificity and accuracy of the native models (vanilla CNN, CNN with under-sampling and CNN with over-sampling) and improved models enhanced by virtual datasets.

	Native model	Undersampling	Oversampling	AVP (600)	AVP (1800)	Random (1800)
<i>Sensitivity</i>	96%	68%	98%	88%	<b>92%</b>	92%
<i>Specificity</i>	18%	48%	26%	<b>52%</b>	<b>66%</b>	38%
<i>Accuracy</i>	<b>57%</b>	58%	62%	<b>70%</b>	<b>79%</b>	65%

associated with specificity and sensitivity of the three classifiers compared with the native classifiers with only the real dataset. The improvement in accuracy using the proposed AVPs is 13% and 22% with 600 and 1800 AVPs, respectively. Meanwhile, both models overcome the imbalance of the real dataset. When using 1800 AVPs, with little compromise in the sensitivity, the specificity increases to 66%, which is almost a four-fold improvement. Furthermore, with the advantages of AVPs mentioned throughout this paper, even a relatively small amount (600) of AVPs can achieve the second-best performance. As for the randomly generated virtual dataset with the size of 1800, the performances for both the classification accuracy and balancing the label distribution are not as good as with AVPs.

## 5.2 Experiments on real medical data

An anonymous image dataset containing 168 patients who underwent a transcatheter aortic valve replacement (TAVR) from 2013 - 2016 is used (Piedmont Healthcare, Atlanta). For each patient, a pre-surgical CT image and the corresponding calcification amount are acquired (see Section 5.2.1 for more details). The learning task is to classify calcification level, which is an important yet challenging clinical problem. Similar to the synthetic experiment, the pathophysiological meaning of GIN and the improvement in classification accuracy using AVPs are of utmost interest. Note that this experiment is only an example and the proposed AVPs have great adaptability to other small data, medicine-related problems.

### 5.2.1 Dataset: TAVR patients

Aortic stenosis (AS) is one of the most common and most serious valvular heart diseases. Transcatheter aortic valve replacement (TAVR) is a less-invasive treatment option for severe AS patients who are at high risk for open-heart surgery. One of the major post-procedural complications of TAVR is the paravalvular leakage (PVL), i.e., the blood flow leakage around the implanted artificial valve due to the incomplete sealing between the implant and the native aortic valve, which is often caused by the *calcifications* presented at the aortic annulus region (a ring-shaped anatomic structure connecting the left ventricle and the aortic valve). Therefore, in clinical practice, the amount and the distribution of annular calcifications are of great importance to predicting the occurrence of post-TAVR PVL. In this experiment, because of the expensive cost of the desired in-vitro PVL experiment (see Section 6), we simplify the task of PVL prediction to the task of calcification evaluation, which is deemed as an important clinical indicator of PVL risk. Due to the variant contrast level in the aortic root and the fast motion of the valve leaflets, it remains challenging to accurately evaluate the calcification near the aortic annulus in pre-TAVR CT images.

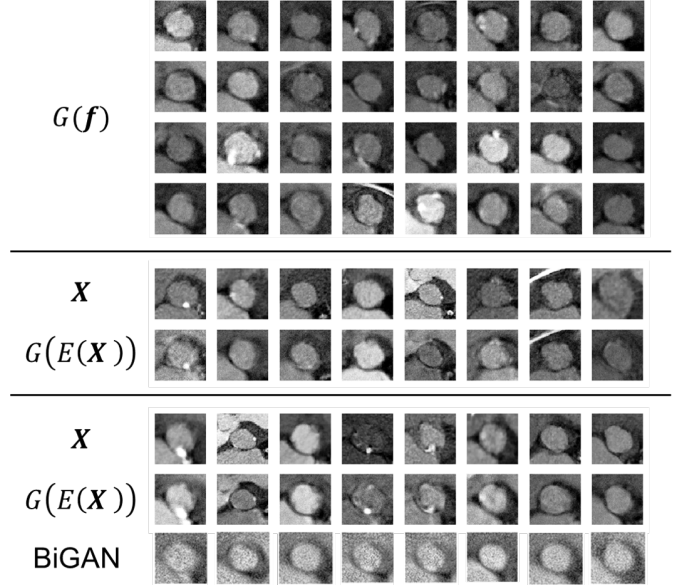


Fig. 7: Qualitative results for GIN training using real CT images at annulus, including the generated samples  $G(\mathbf{f})$ , real data  $\mathbf{X}$ , the corresponding reconstructions  $G(E(\mathbf{X}))$  and the reconstructions by BiGAN [28].

### 5.2.2 Pathophysiological interpretability of GIN

We test the proposed GIN using pre-TAVR CT images at the annulus region. The dimension of the feature space is  $r = 20$ , i.e.,  $\mathbb{F} = [-1, 1]^{20}$ , considering the complexity of real CT images. Detailed architecture of the GIN can be found in Appendix D. Furthermore, a routine data augmentation of rotating (nine total rotations) the original 4D CT of each patient is conducted, resulting in 1680 images as the training set.

**Pathophysiologicaly-interpretable feature space.** In order to better visualize the 20-dimensional feature space  $\mathbb{F} = [-1, 1]^{20}$ , Figure 8 shows a randomly selected 2D cross-section of  $\mathbb{F}$  with the generated virtual valve images located at their projected feature locations. We notice that the variation of the virtual images on the feature grids is continuous and smooth. Meanwhile, we observe that the two axes of the 2D cross-section shown in Figure 8 have pathophysiological meaning. As shown in the red box (enlarged images on the left side), the vertical axis can be interpreted as the change of the calcification (i.e., the regions of high intensity in the CT images) amount. As shown in the blue box (enlarged images on the right side), the horizontal axis can be interpreted as the change of valve shape and the calcification location. Similar observations can be found in the other vertical or horizontal groups of images, which demonstrate the potential pathophysiological interpretability of  $\mathbb{F}$ .

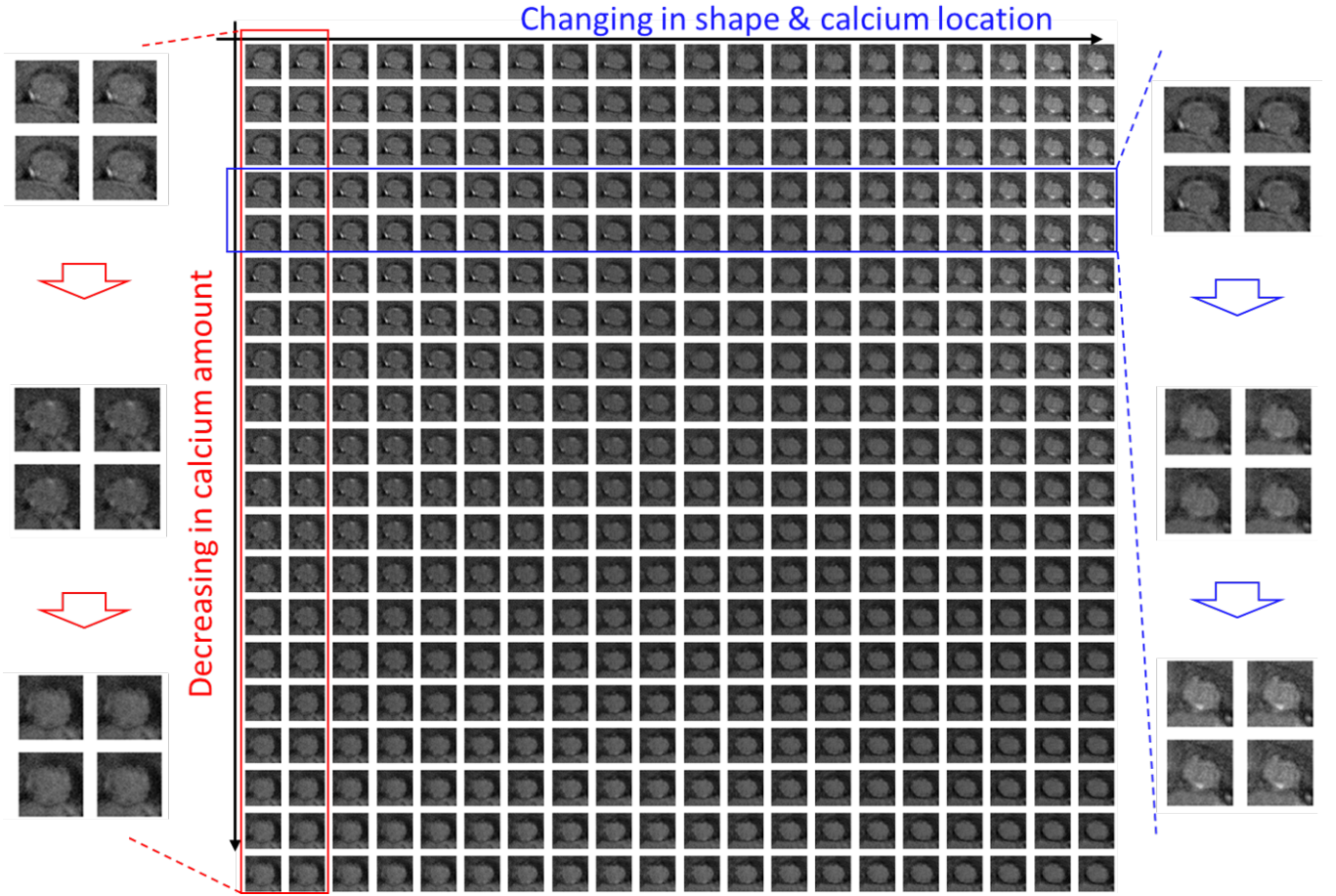


Fig. 8: Qualitative visualization of 2D cross-section of feature space with the generated virtual images on the grid of feature space. The pathophysiological meaning of both axes is visualized in the left and right sides, respectively.

**Reconstruction test.** Similar to the synthetic experiments, a reconstruction test (see Figure 5) is conducted by comparing the real CT images  $X_i$  and the reconstructed virtual images  $\hat{X}_i = G(E(X_i))$ . Figure 7 shows the comparison of the real images and the corresponding reconstructed images. Visually, the reconstructed images are almost identical to the real images with similar background color and valve geometry. Furthermore, the most important pathophysiological indicators, i.e., the location and size of the calcifications are well-recovered. This shows that: (i) using GIN can capture the features of important pathophysiological meaning, and (ii)  $G(\cdot)$  and  $E(\cdot)$  are inverses of each other. Note that the performance of the reconstruction test in Figure 7 is better than that in Figure 3. This is because a more complex model is used and fine tuning is conducted.

**Comparison with BiGAN.** As discussed in Section 2.2, GIN has essentially different objectives compared to BiGAN [28], in which one discriminator is used to supervise both the generator and the encoder. On the contrary, a sequential order of training  $G(\cdot)$  and  $E(\cdot)$  is implemented in the proposed GIN to make sure the sample-to-sample inverse is *explicitly* trained by a strong distance metric of MSE, and therefore, the reconstruction error is minimized even with a limited data size. Nevertheless, we use our data set to train

a BiGAN model<sup>2</sup> for comparison. The last row of Figure 7 shows the reconstruction of the proposed GIN, compared with that of BiGAN using the same real images. Further tuning of the BiGAN is also conducted, with the similar performance (see Figure 4 in [28]). In contrast, the proposed GIN is easier to tune in practice. This is mainly because we separate the training of the generator  $G(\cdot)$  and the encoder  $E(\cdot)$ , and therefore both  $G(\cdot)$  and  $E(\cdot)$  can occupy more resources. As a result, sharper and better reconstruction results are presented with no mode dropping observed even in the small data situation.

### 5.2.3 Improving calcification prediction by AVPs

The learning problem here is to use the CT slide at the annulus to predict the calcification level (see Section 5.2.1). A four-fold cross validation strategy is used (see Appendix D) since only a small dataset is available.

**A native model.** A CNN structure is adapted for the native model (see Appendix D). Table 2 reports the classification accuracy, sensitivity and specificity of the four-fold cross validation using the native model. The prediction accuracy, sensitivity and specificity are low ( $\sim 60\%$ ). The main reason for this is, again, the limited amount of data available.

2. We use official code at <https://github.com/jeffdonahue/biggan>.

TABLE 2: A comparison of classification sensitivity, specificity and accuracy of the native model and improved models enhanced by virtual dataset in a 4-fold cross-validation (see Appendix D). The training size for each model is included.

Fold	Native Model (1260)			Randomly Generated (1260)			$\mu$ -measure design (1260)			Randomly Generated (10126)		
	Accuracy	Sensitivity	Specificity	Accur.	Sensi.	Specif.	Accur.	Sensi.	Specif.	Accur.	Sensi.	Specif.
1	64.29%	52.17%	78.95%	69.05%	60.87%	78.95%	76.19%	73.91%	78.95%	78.57%	78.26%	78.95%
2	57.14%	47.26%	66.67%	64.29%	61.90%	66.67%	73.81%	76.19%	71.43%	76.19%	71.43%	80.95%
3	57.14%	50.00%	63.64%	71.43%	52.94%	84.00%	80.95%	76.47%	84.00%	85.71%	82.35%	88.00%
4	59.52%	55.00%	63.64%	64.29%	60.00%	68.18%	71.43%	75.00%	68.18%	73.81%	70.00%	77.27%
Ave	<b>59.52%</b>	51.11%	68.23%	<b>67.27%</b>	58.93%	74.45%	<b>75.60%</b>	75.39%	75.64%	<b>78.57%</b>	75.51%	81.29%

**Training GIN.** The first step is to learn GIN with the generating mapping  $G(\cdot)$  and the encoding mapping  $E(\cdot)$ . Feature space is set to be  $\mathbb{F} = [-1, 1]^{20}$ . The architecture of GIN is discussed in Appendix D.

**Designing and labeling AVPs.** In this experiment, the dataset is not severely unbalanced, where the ratio of the size of two classes is around 2 : 3. Thus, Equation (8) is used to assign density to the measure  $\mu$  (more details in Appendix D). As for labeling, an empirical approach is performed as the baseline: a mixture model of two Gaussians is used to model the pixel intensity, based on whether the pixels are classified as normal tissues or calcifications. The volume of the calcification region is then calculated. After that, a manual check is performed by a radiologist and the calcification levels are corrected if needed. Three datasets of virtual patients are generated and labeled: AVP with the size 1134 by a  $\mu$ -measure design, and randomly sampled with the size 1134 and 10000. Further discussion of the designed AVPs is included in Appendix E. Note that if budget and time allows, a more sophisticated labeling approach can be used. We provide more discussion in Section 6.

**Classification performance.** The three generated virtual datasets are fused with the real dataset (a total of 126 for every test fold) and three improved classifiers are trained. Note that the native model can be regarded as a baseline with rotation augmentation of 1134 rotated images. Table 2 summarizes the prediction accuracy together with the sensitivity and specificity of the different models. As discussed earlier in this section, the native model performs the poorest over the test set. The prediction accuracy improves when using randomly generated samples with the same data size (126 real + 1134 virtual). This is mainly because additional physical knowledge has been introduced to the virtual dataset by the labeling process, while the native model with the rotating augmentation only adds a rotation-invariant constraint to the model. When using the proposed AVPs, with the same data size (126 real + 1134 AVPs), the model outperforms both the other models. This is not surprising because AVPs are not only located at decision boundaries and they are also optimized for space-fillingness, which achieves better exploration of the feature space with an emphasis in uncertain regions. Furthermore, if we increase the size of the randomly generated virtual dataset to 10000, which may lead to overly expensive labeling costs, the prediction accuracy is higher, but not noticeably higher, than the AVPs dataset with a size of 1260. As a summary, promising results in Table 2 suggest: (i) the physics-based labeling approach in the proposed framework introduces additional physical knowledge as a complement to the small dataset, and therefore yields better prediction performance; (ii) with the same data size, using AVPs achieves a bet-

ter model than either using random sampling or routine rotation augmentation; and (iii) using AVPs with a small data size can reach similar final prediction performance compared to using random sampling with a much bigger data size, which reduces the labeling cost of conducting physical experiments.

## 6 EXTENSION AND FUTURE WORK

Although the aforementioned experiments simplified the clinical task to evaluating the calcification level in the aortic valve, the proposed framework can also be used to predict PVL, which is of more clinical relevance. Different from calcification, the PVL label, considering its hemodynamic nature is difficult to determine via simple empirical methods based on image cues. Moreover, it remains a very challenging task for experienced cardiologists. Therefore, we introduce the idea of *printable* AVPs, which refers to the AVPs with a 3D digital model (i.e., multiple slides of CT images) and can be physically fabricated by 3D printing. Then, in-vitro experimental strategies can be used to acquire the PVL label. We will extend the proposed GIN to generate CT images for printable AVPs in this section, and the further labeling procedure will be discussed while the implement of which will be the focus of future work.

### 6.1 Generating printable AVPs using GIN

In order to generate CT images with multiple slides, the complexity of the GIN should be higher. However, confined by the limited computational power at hand, we use the same architecture for GIN (see Appendix D). The dimension of feature space is set to be  $r = 50$ , i.e.,  $\mathbb{F} = [-1, 1]^{50}$ . We train a GIN using the real CT images dataset. Figure 9 illustrates the generated AVPs and the reconstruction test (see Figure 5), where each row demonstrates one patient represented by the CT slides of different vertical cuts. The generated CT images looks real and sharp. Furthermore, in the reconstruction test, the similarity of the real images and the reconstructed images is high and important pathophysiological features, e.g., calcifications can be captured. Clearly, the generated image is not as sharp as the real CT images. The improvement of this will be the focus of future work. For example, GIN with higher complexity, i.e., more hidden nodes and layers can be used, and deep convolutional architecture [50] can also be tested.

### 6.2 3D printing-based in-vitro experiments

Simple image processing methods (e.g., [49], [51]) can be used to transform the generated AVPs to the 3D digital model. Tissue-mimicking 3D printing technology in the



Fig. 9: Qualitative results for GIN training using real CT images of 24 slides, including five generated samples  $G(f_i)$ , two real data  $X_i, i = 1, 2$  and the corresponding reconstructions  $G(E(X_i))$ .

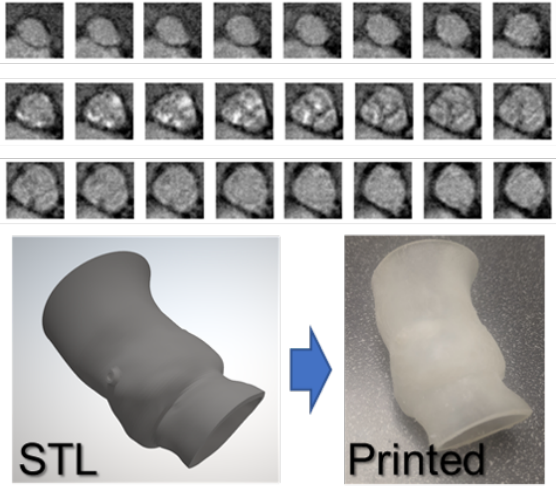


Fig. 10: An example of using tissue-mimicking 3D printing technology to print the generated AVP. The top images are 24 CT slides of a printable AVP (from left to right, top to bottom).

literature [52], [53], which can print phantoms to mimic both the geometry and mechanical property of the biological tissue, can be used to fabricate the AVPs. Then in-vitro experiments will be conducted to acquire accurate PVLs for 3D printed phantoms [44]. The 3D printing-based in-vitro experiments will be the other aspect of our future work. As validated by the two experiments (see Section 5 in this work, we believe the proposed learning framework can improve the prediction accuracy of the PVL, which can be helpful for pre-TAVR surgical planning and reduce the post-TAVR complications.

## 7 CONCLUSION

In this paper, we proposed adaptive virtual patients (AVPs) and the associated physics-based and data-driven framework to improve the prediction performance with limited available data, which is common in medicine-related

learning problems. In the proposed framework, a novel generative neural network – generative invertible networks (GIN) – is proposed to find the bidirectional mapping of generating virtual patients and extracting the features of the real ones. An important contribution of the proposed framework is to incorporate domain-specific knowledge into the labeling process of the generated AVPs. This can be crucial in improving the prediction accuracy when only a small and sometimes unbalanced dataset is available. Furthermore, a  $\mu$ -measure design is conducted to properly explore the whole feature space by smartly sampling the AVPs, which not only focuses on the uncertain regions of the native model but also balances the label distribution. By doing that, in a real medical case study of predicting aortic calcification, high prediction accuracy ( $> 75\%$ ) can be achieved with a small training set ( $\sim 100$ ) and a relatively small amount of AVPs ( $\sim 1000$ ). This is a noticeable increase in accuracy of 15% and reduction in labeling cost of 90%. Furthermore, the proposed framework has great adaptability to different medicine-related learning problems. Specifically, the possibility of predicting post-TAVR PVL is discussed and will be the focus of our future work.

## ACKNOWLEDGMENTS

The authors would like to thank Dr. Shizhen Liu at Piedmont Heart Institute in Atlanta, GA, for providing medical knowledge. The authors also want to thank Dr. Zih Hwei Wang at Feng Chia University and Mr. Geet Lahoti at Georgia Tech for the insightful discussions.

## REFERENCES

- [1] I. Goodfellow, Y. Bengio, A. Courville, and Y. Bengio, *Deep learning*. MIT press Cambridge, 2016, vol. 1.
- [2] Y. LeCun, K. Kavukcuoglu, C. Farabet *et al.*, “Convolutional networks and applications in vision.” in *ISCAS*, vol. 2010, 2010, pp. 253–256.
- [3] D. Bahdanau, K. Cho, and Y. Bengio, “Neural machine translation by jointly learning to align and translate,” *arXiv preprint arXiv:1409.0473*, 2014.
- [4] A. Esteva, B. Kuprel, R. A. Novoa, J. Ko, S. M. Swetter, H. M. Blau, and S. Thrun, “Dermatologist-level classification of skin cancer with deep neural networks,” *Nature*, vol. 542, no. 7639, p. 115, 2017.



- [5] G. Litjens, T. Kooi, B. E. Bejnordi, A. A. A. Setio, F. Ciompi, M. Ghafoorian, J. A. Van Der Laak, B. Van Ginneken, and C. I. Sánchez, "A survey on deep learning in medical image analysis," *Medical image analysis*, vol. 42, pp. 60–88, 2017.
- [6] S. S. Du, Y. Wang, X. Zhai, S. Balakrishnan, R. Salakhutdinov, and A. Singh, "How many samples are needed to learn a convolutional neural network?" *arXiv preprint arXiv:1805.07883*, 2018.
- [7] H. He and E. A. Garcia, "Learning from imbalanced data," *IEEE Transactions on Knowledge & Data Engineering*, no. 9, pp. 1263–1284, 2008.
- [8] N. V. Chawla, N. Japkowicz, and A. Kotcz, "Special issue on learning from imbalanced data sets," *ACM Sigkdd Explorations Newsletter*, vol. 6, no. 1, pp. 1–6, 2004.
- [9] M. Raissi, P. Perdikaris, and G. E. Karniadakis, "Physics informed deep learning (part i): Data-driven solutions of nonlinear partial differential equations," *arXiv preprint arXiv:1711.10561*, 2017.
- [10] M. Raissi and G. E. Karniadakis, "Hidden physics models: Machine learning of nonlinear partial differential equations," *Journal of Computational Physics*, vol. 357, pp. 125–141, 2018.
- [11] V. R. Joseph and H. Yan, "Engineering-driven statistical adjustment and calibration," *Technometrics*, vol. 57, no. 2, pp. 257–267, 2015.
- [12] A. Gelman, J. B. Carlin, H. S. Stern, and D. B. Rubin, *Bayesian data analysis*. Chapman and Hall/CRC, 1995.
- [13] S. Mak, C.-L. Sung, X. Wang, S.-T. Yeh, Y.-H. Chang, V. R. Joseph, V. Yang, and C. J. Wu, "An efficient surrogate model for emulation and physics extraction of large eddy simulations," *Journal of the American Statistical Association*, pp. 1–14, 2018.
- [14] J. Chen, S. Mak, V. R. Joseph, and C. Zhang, "A functional-input, functional-output emulation model for efficient tissue-mimicking via 3D-printed metamaterial," *Journal of the American Statistical Association*, Submitted.
- [15] Y. LeCun, Y. Bengio, and G. Hinton, "Deep learning," *nature*, vol. 521, no. 7553, p. 436, 2015.
- [16] I. Goodfellow, J. Pouget-Abadie, M. Mirza, B. Xu, D. Warde-Farley, S. Ozair, A. Courville, and Y. Bengio, "Generative adversarial nets," in *Advances in neural information processing systems*, 2014, pp. 2672–2680.
- [17] A. Fagraeus *et al.*, "Antibody production in relation to the development of plasma cells. in vivo and in vitro experiments." *Acta Medica Scandinavica*, vol. 130, no. Suppl. 204, 1948.
- [18] J. D. Anderson and J. Wendt, *Computational fluid dynamics*. Springer, 1995, vol. 206.
- [19] S. Barry Issenberg, W. C. McGaghie, E. R. Petrusa, D. Lee Gordon, and R. J. Scalese, "Features and uses of high-fidelity medical simulations that lead to effective learning: a beme systematic review," *Medical teacher*, vol. 27, no. 1, pp. 10–28, 2005.
- [20] B. J. Winer, "Statistical principles in experimental design." 1962.
- [21] K. Chatfield, K. Simonyan, A. Vedaldi, and A. Zisserman, "Return of the devil in the details: Delving deep into convolutional nets," *arXiv preprint arXiv:1405.3531*, 2014.
- [22] J. Chen, Y. Xie, K. Wang, Z. H. Wang, G. Lahoti, C. Zhang, M. A. Vannan, B. Wang, and Z. Qian, "Generative invertible networks (gin): Pathophysiology-interpretable feature mapping and virtual patient generation," in *International Conference on Medical Image Computing and Computer-Assisted Intervention*. Springer, 2018, pp. 537–545.
- [23] S. J. Pan, Q. Yang *et al.*, "A survey on transfer learning," *IEEE Transactions on knowledge and data engineering*, vol. 22, no. 10, pp. 1345–1359, 2010.
- [24] J.-Y. Zhu, T. Park, P. Isola, and A. A. Efros, "Unpaired image-to-image translation using cycle-consistent adversarial networks," *arXiv preprint*, 2017.
- [25] P. Isola, J.-Y. Zhu, T. Zhou, and A. A. Efros, "Image-to-image translation with conditional adversarial networks," *arXiv preprint*, 2017.
- [26] M. Mirza and S. Osindero, "Conditional generative adversarial nets," *arXiv preprint arXiv:1411.1784*, 2014.
- [27] V. Dumoulin, I. Belghazi, B. Poole, O. Mastropietro, A. Lamb, M. Arjovsky, and A. Courville, "Adversarially learned inference," *arXiv preprint arXiv:1606.00704*, 2016.
- [28] J. Donahue, P. Krähenbühl, and T. Darrell, "Adversarial feature learning," *arXiv preprint arXiv:1605.09782*, 2016.
- [29] C. J. Wu and M. S. Hamada, *Experiments: planning, analysis, and optimization*. John Wiley & Sons, 2011, vol. 552.
- [30] T. J. Santner, B. J. Williams, and W. I. Notz, *The design and analysis of computer experiments*. Springer Science & Business Media, 2013.
- [31] S. I. Resnick, *A Probability Path*. Springer Science & Business Media, 2013.
- [32] C. Villani, *Optimal transport: old and new*. Springer Science & Business Media, 2008, vol. 338.
- [33] A. Rakotomamonjy, A. Traore, M. Berar, R. Flamary, and N. Courty, "Wasserstein distance measure machines," *arXiv preprint arXiv:1803.00250*, 2018.
- [34] J.-D. Benamou, G. Carlier, M. Cuturi, L. Nenna, and G. Peyré, "Iterative bregman projections for regularized transportation problems," *SIAM Journal on Scientific Computing*, vol. 37, no. 2, pp. A1111–A1138, 2015.
- [35] Y. Xie, X. Wang, R. Wang, and H. Zha, "A fast proximal point method for wasserstein distance," *arXiv preprint arXiv:1802.04307*, 2018.
- [36] M. Arjovsky, S. Chintala, and L. Bottou, "Wasserstein gan," *arXiv preprint arXiv:1701.07875*, 2017.
- [37] E. A. Nadaraya, "On estimating regression," *Theory of Probability & its Applications*, vol. 9, no. 1, pp. 141–142, 1964.
- [38] G. Matheron, "Principles of geostatistics," *Economic Geology*, vol. 58, no. 8, pp. 1246–1266, 1963.
- [39] X. Xian, A. Wang, and K. Liu, "A nonparametric adaptive sampling strategy for online monitoring of big data streams," *Technometrics*, vol. 60, no. 1, pp. 14–25, 2018.
- [40] D. Busby, "Hierarchical adaptive experimental design for gaussian process emulators," *Reliability Engineering & System Safety*, vol. 94, no. 7, pp. 1183–1193, 2009.
- [41] S. Mak, V. R. Joseph *et al.*, "Support points," *The Annals of Statistics*, vol. 46, no. 6A, pp. 2562–2592, 2018.
- [42] W. R. Gilks, S. Richardson, and D. Spiegelhalter, *Markov chain Monte Carlo in practice*. Chapman and Hall/CRC, 1995.
- [43] S. Mak and V. R. Joseph, "Projected support points, with application to optimal mcmc reduction," *arXiv preprint arXiv:1708.06897*, 2017.
- [44] Z. Qian, K. Wang, S. Liu, X. Zhou, V. Rajagopal, C. Meduri, J. R. Kauten, Y.-H. Chang, C. Wu, C. Zhang *et al.*, "Quantitative prediction of paravalvular leak in transcatheter aortic valve replacement based on tissue-mimicking 3d printing," *JACC: Cardiovascular Imaging*, vol. 10, no. 7, pp. 719–731, 2017.
- [45] O. C. Zienkiewicz, R. L. Taylor, O. C. Zienkiewicz, and R. L. Taylor, *The finite element method*. McGraw-hill London, 1977, vol. 36.
- [46] P. A. Thompson and S. M. Troian, "A general boundary condition for liquid flow at solid surfaces," *Nature*, vol. 389, no. 6649, p. 360, 1997.
- [47] J. Kuruvilla and K. Gunavathi, "Lung cancer classification using neural networks for ct images," *Computer methods and programs in biomedicine*, vol. 113, no. 1, pp. 202–209, 2014.
- [48] P. Loughna, L. Chitty, T. Evans, and T. Chudleigh, "Fetal size and dating: charts recommended for clinical obstetric practice," *Ultrasound*, vol. 17, no. 3, pp. 160–166, 2009.
- [49] A. Bardera, I. Boada, M. Feixas, and M. Sbert, "Image segmentation using excess entropy," *Journal of Signal Processing Systems*, vol. 54, no. 1-3, pp. 205–214, 2009.
- [50] A. Radford, L. Metz, and S. Chintala, "Unsupervised representation learning with deep convolutional generative adversarial networks," *arXiv preprint arXiv:1511.06434*, 2015.
- [51] R. I. Ionasec, I. Voigt, B. Georgescu, Y. Wang, H. Houle, F. Vega-Higuera, N. Navab, and D. Comaniciu, "Patient-specific modeling and quantification of the aortic and mitral valves from 4-d cardiac ct and tee," *IEEE Transactions on Medical Imaging*, vol. 29, no. 9, pp. 1636–1651, 2010.
- [52] K. Wang, Y. Zhao, Y.-H. Chang, Z. Qian, C. Zhang, B. Wang, M. A. Vannan, and M.-J. Wang, "Controlling the mechanical behavior of dual-material 3d printed meta-materials for patient-specific tissue-mimicking phantoms," *Materials & Design*, vol. 90, pp. 704–712, 2016.
- [53] J. Chen, K. Wang, C. Zhang, and B. Wang, "An efficient statistical approach to design 3d-printed metamaterials for mimicking mechanical properties of soft biological tissues," *Additive Manufacturing*, vol. 24, pp. 341–352, 2018.

## APPENDIX A

### PROOF OF THEOREM 1.

Since the generator  $G(\cdot)$  is obtained by (5) with the training error  $< \epsilon$ , i.e.,

$$\mathcal{W}(\mathcal{X}, G_{\#}[\mathcal{U}]) = \inf_{\gamma} \int_{\mathbb{X} \times \mathbb{X}} \|x - G(u)\|_2 d\gamma(x, G(u)) = d < \epsilon. \quad (13)$$

This means we have obtained the transportation map  $\gamma : \mathbb{X} \times \mathbb{X} \mapsto [0, 1]$ , s.t.,

$$\mathbb{E}_{\gamma}[\|X - G(U)\|_2] = \int \|x - G(u)\|_2 d\gamma(x, G(u)) = d, \quad (14)$$

For any realization  $x_i \in \mathbb{X}$  of the random variable  $X \sim \mathcal{X}$ , one can find a  $u_i \in \mathbb{F}$  using the following optimization scheme:

$$u_i = \operatorname{argmin}_{u \in \mathbb{F}} \|x_i - G(u)\|_2, \quad (15)$$

We denote this as  $u_i = h(x_i)$ . If we denote the conditional measure of  $\gamma$  as  $\gamma_{x_i} = \gamma|X = x_i$ . Given  $X = x_i$  and  $u_i = h(x_i)$ , clearly, we have,

$$\|x_i - G(u_i)\|_2 \leq \mathbb{E}_{U \sim \gamma_{x_i}} \|x_i - G(U)\|_2, \quad (16)$$

Furthermore, recall the dual formula of the Wasserstein distance:

$$\mathcal{W}(\mathcal{X}, G_{\#}[\mathcal{U}]) = \sup_{\|D(\cdot)\|_L \leq 1} \mathbb{E}_{x \sim \mathcal{X}}[D(x)] - \mathbb{E}_{u \sim \mathcal{U}}[D(G(u))] < \epsilon, \quad (17)$$

Specifically, if let the function  $D(x) = h(x) - E(x)$ , we have :

$$\|\mathbb{E}_{x \sim \mathcal{X}}[h(x) - E(G(h(x)))] - \mathbb{E}_{u \sim \mathcal{U}}[u - E(G(u))]\| < \epsilon, \quad (18)$$

With  $x_i, u_i$  and the Lipschitz-L continues assumption on  $G(\cdot)$ , we have:

$$\|G(E(x_i)) - x_i\|_2 \leq \|G(E(x_i)) - G(u_i)\|_2 + \|G(u_i) - x_i\|_2 \leq L\|E(x_i) - u_i\|_2 + \|G(u_i) - x_i\|_2 \quad (19)$$

Now, replace the realization  $x_i$  with the random variable  $X$  and take the expectation over  $X \sim \mathcal{X}$ ,

$$\mathbb{E}_{X \sim \mathcal{X}} \|G(E(X)) - X\|_2 \leq L\mathbb{E}_{X \sim \mathcal{X}} \|E(X) - h(X)\|_2 + \mathbb{E}_{X \sim \mathcal{X}} \|G(h(X)) - X\|_2. \quad (20)$$

Considering the way we choose  $u_i = h(X_i)$  and the inequality (16), for the second term above, we have

$$\mathbb{E}_{X \sim \mathcal{X}} \|X - G(h(X))\|_2 \leq \mathbb{E}_{X \sim \mathcal{X}} \mathbb{E}_{U \sim \gamma_X} \|X - G(U)\|_2 = \mathbb{E}_{\gamma} \|X - G(U)\|_2 \leq \epsilon \quad (21)$$

As for the first term, we have:

$$\mathbb{E}_{X \sim \mathcal{X}} \|E(X) - h(X)\|_2 \leq \mathbb{E}_{X \sim \mathcal{X}} \|E(X) - E(G(U))\|_2 + \mathbb{E}_{X \sim \mathcal{X}} \|h(X) - E(G(U))\|_2 \quad (22)$$

With the Lipschitz-L continues assumption on  $E(\cdot)$ :

$$\mathbb{E}_{X \sim \mathcal{X}} \|E(X) - h(X)\|_2 \leq L\mathbb{E}_{X \sim \mathcal{X}} \|X - G(U)\|_2 + \mathbb{E}_{X \sim \mathcal{X}} \|h(X) - E(G(U))\|_2 \leq L\epsilon + \mathbb{E}_{X \sim \mathcal{X}} \|h(X) - E(G(U))\|_2 \quad (23)$$

Note that  $E(\cdot)$  is obtained by (7) with training error  $\mathbb{E}_{U \sim \mathcal{U}} [\|E(G(U)) - U\|_2] < \delta$ . Recall Equation (18),

$$\mathbb{E}_{X \sim \mathcal{X}} \|U - E(G(U))\|_2 \leq \mathbb{E}_{U \sim \mathcal{U}} \|U - E(G(U))\|_2 + \epsilon \leq \delta + \epsilon \quad (24)$$

Finally, we have

$$\mathbb{E}_{X \sim \mathcal{X}} \|G(E(X)) - X\|_2 \leq L(L\epsilon + \delta + \epsilon) + \epsilon = (L^2 + L + 1)\epsilon + L\delta. \quad (25)$$

## APPENDIX B

### PROOF OF THEOREM 2.

we denote the target measure as  $\mathcal{X}$  with its empirical representation as  $\mathcal{X}_n$ , while  $\tilde{\mathcal{X}}$  as measure obtained by proposed approach with its empirical representation as  $\tilde{\mathcal{X}}_n$ .

(i) As the training data size approach infinity,  $\tilde{\mathcal{X}}_n \rightarrow \mathcal{X}_n$ , this because using Pinskers inequality,

$$\left| \sum_{x_i \in \mathcal{D}} \mathcal{I}(x_i > y) - \sum_{\tilde{x}_i \in \tilde{\mathcal{D}}} \mathcal{I}(\tilde{x}_i > y) \right| < \sqrt{KL(\tilde{\mathcal{X}}_n || \mathcal{X}_n)}. \quad (26)$$

where  $KL(\cdot || \cdot)$  is the K-L divergence of two distribution. From [36], we know the  $KL(\tilde{\mathcal{X}}_n || \mathcal{X}_n) \rightarrow 0$  as  $n \rightarrow \infty$ , i.e., existing a small  $\epsilon > 0$ , for any  $y$ ,

$$\left| \sum_{x_i \in \mathcal{D}} \mathcal{I}(x_i > y) - \sum_{\tilde{x}_i \in \tilde{\mathcal{D}}} \mathcal{I}(\tilde{x}_i > y) \right| < \frac{\epsilon}{3}. \quad (27)$$

For more discussion and justification, please refer to [36].

(ii) As the data size approach infinity,  $\mathcal{X}_n \rightarrow \mathcal{X}$ . Since the training dataset  $\mathcal{D} = \{x_i\}_{i=1}^n$  is sampled from the target measure  $\mathcal{X}$ , its empirical CDF converges to target CDF  $F_{\mathcal{X}}$ , i.e., for any  $y$ ,

$$\left| \sum_{x_i \in \mathcal{D}} \mathcal{I}(x_i > y) - F_{\mathcal{X}}(y) \right| < \frac{\epsilon}{3}. \quad (28)$$

(iii) Similar to (ii), as the data size approach infinity,  $\left| \sum_{\tilde{x}_i \in \tilde{\mathcal{D}}} \mathcal{I}(\tilde{x}_i > y) - F_{\tilde{\mathcal{X}}}(y) \right| < \epsilon/3$ .

We have the difference in the obtained CDF and the target CDF:

$$|F_{\mathcal{X}}(y) - F_{\tilde{\mathcal{X}}}(y)| = \left| F_{\mathcal{X}}(y) - \sum_{x_i \in \mathcal{D}} \mathcal{I}(x_i > y) + \sum_{x_i \in \mathcal{D}} \mathcal{I}(x_i > y) - \sum_{\tilde{x}_i \in \tilde{\mathcal{D}}} \mathcal{I}(\tilde{x}_i > y) + \sum_{\tilde{x}_i \in \tilde{\mathcal{D}}} \mathcal{I}(\tilde{x}_i > y) - F_{\tilde{\mathcal{X}}}(y) \right|. \quad (29)$$

Combining (i), (ii) and (iii), we know as the training data size large enough, with any  $y$ ,

$$|F_{\mathcal{X}}(y) - F_{\tilde{\mathcal{X}}}(y)| \leq \left| F_{\mathcal{X}}(y) - \sum_{x_i \in \mathcal{D}} \mathcal{I}(x_i > y) \right| + \left| \sum_{x_i \in \mathcal{D}} \mathcal{I}(x_i > y) - \sum_{\tilde{x}_i \in \tilde{\mathcal{D}}} \mathcal{I}(\tilde{x}_i > y) \right| + \left| \sum_{\tilde{x}_i \in \tilde{\mathcal{D}}} \mathcal{I}(\tilde{x}_i > y) - F_{\tilde{\mathcal{X}}}(y) \right| < \epsilon. \quad (30)$$

i.e., as the training data size approach infinity,  $\tilde{\mathcal{X}} \rightarrow \mathcal{X}$  in distribution.

## APPENDIX C

### PROOF OF THEOREM 3.

According to Equation (11), we construct the measure  $\mu$  with density:

$$f_{\mu}(z) = \begin{cases} b_1 \exp(-\theta_1(c(z) - TH)) & \text{if } c(z) \geq TH; \\ b_0 \exp(-\theta_0(c(z) - TH)) & \text{if } c(z) < TH, \end{cases} \quad (31)$$

and the hyperparameters  $\theta_1, \theta_2, b_1$  and  $b_2$  are selected such that the probability over the two class are both 0.5:

$$\int_{\mathbb{F}_0} f_{\mu}(z) dz = \int_{\mathbb{F}_1} f_{\mu}(z) dz = \frac{1}{2}, \quad (32)$$

where, subset  $\mathbb{F}_0 = \{z \in \mathbb{F} : C(G(z)) < TH\}$  and subset  $\mathbb{F}_1 = \{z \in \mathbb{F} : C(G(z)) \geq TH\}$ .

Note that we are using SPs to generate sample from measure  $\mu$ . From Proposition 1, we know that the empirical CDF of  $\hat{\mu}$  represented by data points  $\mathcal{D}_a = \mathcal{D} \cup \tilde{\mathcal{D}}$  converge to the CDF of  $\mu$  as  $m \rightarrow \infty$ , i.e., with any  $y$ ,

$$\sum_{\mathbf{X}_i \in \mathcal{D}_a} \frac{\mathcal{I}(C(\mathbf{X}_i) > y)}{|\mathcal{D}_a|} \rightarrow F_{\mu}(y). \quad (33)$$

Since  $\mu$  is balanced over the two classes  $\frac{\int_{\mathbb{F}_0} f_{\mu}(z) dz}{\int_{\mathbb{F}_1} f_{\mu}(z) dz} = 1$ , we have

$$\frac{\sum_{\mathbf{X}_i \in \mathcal{D}_a} \mathcal{I}(C(\mathbf{X}_i) > TH)}{\sum_{\mathbf{X}_i \in \mathcal{D}_a} \mathcal{I}(C(\mathbf{X}_i) < TH)} = 1, \quad (34)$$

as  $m \rightarrow \infty$ , with probability 1.

## APPENDIX D

### DETAILS OF THE IMPLEMENTATION

**Architecture of GIN.** For the synthetic dataset, the generator  $G(\cdot)$  adapts 5-layer vanilla NN with 512, 512, 1024, 1024, 1024 hidden nodes in each hidden layer, respectively, and ReLu activation. The discriminator  $D(\cdot)$  also adapts 5-layer vanilla NN with 1024, 1024, 1024, 512, 512 hidden nodes, and ReLu activation. As for the encoder  $E(\cdot)$ , it has 16 convolutional layers with 128, 256, 256, 256, 512, 512, 512, 512, 1024, 1024, 2048, 2048, 1024, 1024, 512, 256 hidden nodes in each hidden layer, respectively, leaky ReLu activation and batch normalization (see [50] for more details). For the real medical dataset, the architecture of GIN is similar to the above one, except that the numbers of the hidden nodes are all doubled.

**Architecture of the native model and improved model.** For the synthetic dataset, both the native model  $C(\cdot)$  and the improved model  $C^*(\cdot)$  have two convolutional layers with 32 and 128 hidden nodes, respectively. Leaky ReLu activation and batch normalization are also included in each layer. After the convolutional layers, three fully connected layers with 64, 32, 16 hidden nodes are used, respectively, with ReLu activation. MSE is used as the loss function and the threshold separating the two classes is set to be  $TH = 0.5$ . For the real medical dataset,  $C(\cdot)$  and  $C^*(\cdot)$  both have the similar three convolutional layers with leaky ReLu activation and batch normalization. The three convolutional layers have 32, 64 and 128 hidden nodes, respectively. After the convolutional layers, three fully connected layers with 128, 64 and 32 hidden nodes are used, respectively, with ReLu activation. MSE is used as the loss function and the threshold separating the two

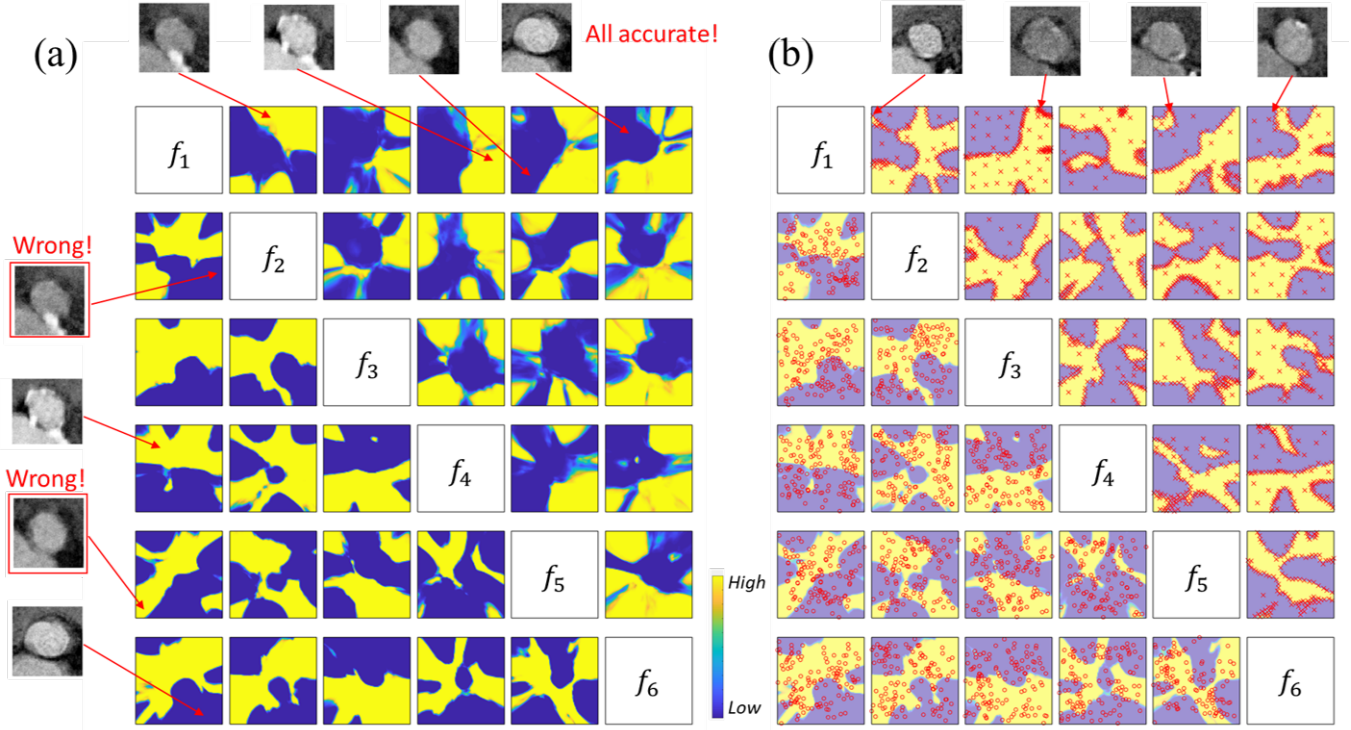


Fig. 11: (a) A compression of the classification model of the native model (bottom left) and the improved model (top right) enhanced by AVP on the 6D feature space  $\mathbb{F}$ . Four testing images are shown and the native model can only correctly classify two of them, while the improved model can correctly classify all of them. (b) A compression of the real patients (bottom left) and AVP (top right) in the feature space. Four examples of the generated AVPs are also shown.

classes is set to be  $TH = 0.5$ . Note that the complexity for both  $C(\cdot)$  and  $C^*(\cdot)$  is low, especially compared to the encoder  $E(\cdot)$ . This is mainly because that the dimensionality of the classification problem is much lower than that of the regression problem for  $E(\cdot)$ . Also, the training set for  $C(\cdot)$  and  $C^*(\cdot)$  is much smaller than that for  $E(\cdot)$ .

**Hyperparameters in  $\mu$ -measure design.** For the synthetic dataset, the hyperparameters in (10) are chosen to be  $\theta_1 = 17$  and  $\theta_0 = 6$ . The integral constants are selected  $b_0 = b_1 = b$ , whose value is set to make sure  $\int f_\mu(z)dz = 1$ . The reason for choosing those parameters follows the heuristic trial-and-error strategy. Note that in the above setting, we are not balancing the dataset according to Equation (11). This is because the native model  $C(\cdot)$  is quite inaccurate as shown in Table 1. Thus, besides balancing the label distribution, we also want to explore the whole feature space using some portion of the AVPs to improve the overall performance. For the real medical dataset, we set the hyperparameter  $\theta = 1000$ , and  $b$  is selected accordingly as an integral constant. Compared with the synthetic experiment, here  $\theta$  is set to be higher to accommodate the increased dimension in the feature space. Meanwhile, in this test, we want to focus more on the boundary (rather than only space-filling), where the most of the uncertainty locates.

**Four-fold cross validation.** Four-fold cross validation on the rotationally augmented data ( $168 \times 10 = 1680$ ) is conducted in the experiment of real medical set. Specifically, three quarters of the existing data ( $168 \times 75\% \times 10 = 1260$ ) after rotation data augmentation is used as the training set while the remaining quarter ( $168 \times 25\% = 42$ ) will be the testing set. Since the architecture of the classifier is pre-defined and there is no hyperparameters need to be tuned, the validation set is not needed.

## APPENDIX E

### A VISUALIZATION OF IMPROVING CLASSIFICATION ACCURACY BY AVPs.

In order to better visualize the sampled AVPs and demonstrate how it helps in improving the classification accuracy, we conduct the experiments in the Section 5.2.3 with the dimension of the feature space  $r = 6$ , i.e.,  $\mathbb{F} = [-1, 1]^6$ .

With the obtained native model  $C(\cdot)$  from Section 5.2.3 and the  $G(\cdot)$  and  $E(\cdot)$  with  $\mathbb{F} = [-1, 1]^6$ , we can visualize  $C(\cdot)$  by using the mapping  $C(G(\cdot)) : \mathbb{F} \mapsto [0, 1]$ . The prediction contour  $C(G(\cdot))$  of the model learned by the first three folds of the training data (the remain fold is for testing) is shown in lower left half of Figure 11 (a). Every small figure visualizes a 2D subspace of  $\mathbb{F}$  with the remaining features set to be zero. Note that all combination of the two features (totally 15 for 6 features) are shown in lower left half of Figure 11 (a). Yellow means high calcification amount (i.e.,  $C(G(f)) = 1$ ), while blue means low calcification amount (i.e.,  $C(G(f)) = 0$ ). Meanwhile, four testing valves are shown in the left side of Figure 11 (a). The obtained native model  $C(\cdot)$  only accurately classifies two of them, which indicates the native model needs improvement.



Designed AVPs are shown in upper left region of Figure 11 (b). Note that for every figure, only 10% of the AVPs closest to the 2D cross-section plane are included for better visualization purpose. Most of AVPs, as expected, are located on the boundary of the prediction contour of the native model, while the rest design points are uniformly dispersed over the whole space. Four examples of the designed AVPs are also visualized on the top, with an arrow pointing its feature in the feature space. Visually, they are indeed confusing for predicting the calcification amount. After physical labeling by a radiologist, they will be helpful in improving the classifier. As a comparison, the real patients (totally, 126) projected in every 2D cross-section are shown in the lower right region of Figure 11 (b). Note that the real patients are randomly distributed in the whole 6D space with no clear pattern.

The prediction contour  $C^*(G(\cdot))$  of the improved classifier  $C^*(\cdot)$  using AVPs is shown in the top left half of Figure 11 (a). We can see finer structure is learned indicating a more sophisticated model is obtained. Meanwhile, the four characteristic valves tested by the native model is also test by the  $C^*(\cdot)$ . The classification of all four are accurate, showing the noticeable improvement in the prediction accuracy by AVPs.